Global and Planetary Change 229 (2023) 104241

Contents lists available at ScienceDirect

Global and Planetary Change

journal homepage: www.elsevier.com/locate/gloplacha

Eustatic change across the Paleocene-Eocene Thermal Maximum in the epicontinental Tarim seaway

Jingxin Jiang [a], Xiumian Hu [a,*], Juan Li [a,b], Eduardo Garzanti [c], Shijun Jiang [d], Ying Cui [e], Yasu Wang [d]

[a] State Key Laboratory of Mineral Deposit Research, School of Earth Sciences and Engineering, Nanjing University, Nanjing 210023, China
[b] Nanjing Institute of Geology and Paleontology, Chinese Academy of Sciences, Nanjing 210008, China
[c] Laboratory for Provenance Studies, Department of Earth and Environmental Sciences, Università di Milano-Bicocca, Milano 20126, Italy
[d] College of Oceanography, Hohai University, Nanjing 210024, China
[e] Department of Earth and Environmental Studies, Montclair State University, Montclair, NJ 07043, USA

ARTICLE INFO

Editor: Dr. Fabienne Marret-Davies

Keywords:
PETM
Carbon-isotope stratigraphy
Microfacies analysis
Glaciers melting
Thermal expansion
Tarim Sea

ABSTRACT

The Paleocene-Eocene Thermal Maximum (PETM) offers an excellent opportunity to study the ecological and environmental responses to global warming. Discussing the so far poorly constrained amplitude and mechanisms of sea-level changes during the PETM is the principal goal of the present study from the epicontinental Tarim seaway. A negative carbon isotope excursion precisely constrains the stratigraphic position of the PETM event within the Qimugen Formation. Microfacies data show that tidal and lagoonal carbonates or sandstone characterizing the Tarim seaway in the pre-PETM stage were gradually replaced by open-marine to middle-ramp marlstones at PETM onset, by outer-ramp mudrocks in the *syn*-PETM stage, and eventually by middle-ramp carbonates in the post-PETM stage. A deepening paleo-water depth trend documents a transgressive sequence leading to maximum flooding during PETM peak. The content of planktonic foraminifera in Qimugen Formation sediments deposited below storm wave base indicates a minimum paleo-water depth of 20–50 m. Regional and global comparisons of sea-level curves suggest that this sea level rise documented in the Tarim epicontinental seaway during the PETM is a largely eustatic consequence of global warming, inducing extensive melting of high-mountain glaciers and thermal expansion of sea water.

1. Introduction

The Paleocene-Eocene Thermal Maximum (PETM) was a short-lived climatic event, occurred around 56 Ma and lasted ~170 to 200 kyr, when the temperature of surface ocean waters rose by 5–8 °C (Kennett and Stott, 1991; Zachos et al., 2001; McInerney and Wing, 2011; Hu et al., 2020; Westerhold et al., 2020; Tierney et al., 2022). The PETM onset was marked by a large (~ 3–6‰) negative carbon-isotope excursion (CIE), caused by the injection of 2000 to >13,000 billion tonnes of ^{13}C-depleted carbon into the ocean-atmosphere system (Dupuis et al., 2003; Panchuk et al., 2008; Cui et al., 2011; McInerney and Wing, 2011; Gutjahr et al., 2017). The sources of such light-carbon emission and the triggering mechanisms of the PETM event are hotly debated. Leading hypotheses involve the release of methane hydrates (Dickens et al., 1997; Minshull et al., 2016), volcanic-gas emissions during emplacement of the North Atlantic igneous province (Svensen et al., 2004; Jones et al., 2019; Berndt et al., 2023), or astronomical forcing (Zeebe and Lourens, 2019; Li et al., 2022). The PETM exerted a profound influence on ecological and sedimentary systems, and caused severe environmental changes including acidification of ocean waters (Zachos et al., 2005), anoxia (Yao et al., 2018), and faunal extinctions and migrations in terrestrial and marine ecosystems (Wing et al., 2005; Speijer et al., 2012; Vitek et al., 2021).

As the most dramatic climatic event of the Cenozoic, the PETM is widely considered to provide the best analogue for studying the ecological and environmental responses to present-day global warming associated with eustatic rise. Sea-level change during the PETM has been documented in many regions worldwide by paleontological assemblages (e.g., foraminifera, pollen, ostracods), geochemical proxies (e.g., terrigenous organic carbon, Y/Ho ratio), grain-size trends, and microfacies analysis, all consistently pointing to widespread transgression (see Sluijs et al., 2008 for a review). Schmitz and Pujalte (2003) suggested

* Corresponding author.
E-mail address: huxm@nju.edu.cn (X. Hu).

https://doi.org/10.1016/j.gloplacha.2023.104241
Received 28 February 2023; Received in revised form 5 September 2023; Accepted 7 September 2023
Available online 9 September 2023

that enhanced hinterland erosion during the PETM in the Pyrenees was related to increased fluvial incision as a consequence of sea-level fall, although an enhanced hydrological cycle offers a plausible alternative (Li et al., 2021a; Pujalte et al., 2022). Overall, the view that sea levels was rising during the PETM is widely accepted, but only a limited number of studies have discussed the potential controlling mechanisms, including thermal expansion of seawater, melting from small-scale Antarctic glaciers, and decrease in the volume of oceanic basins (Sluijs et al., 2008; Harris et al., 2010). The aquifer eustasy hypothesis, which has garnered considerable attention recently (Sames et al., 2020; Li et al., 2023), has not been thoroughly examined in the PETM case.

Detailed stratigraphic and sedimentological studies are needed to better constrain the amplitude of eustatic change during the PETM, which remains poorly understood. Shallow seas, and particularly epicontinental seas, are highly sensitive to fluctuations in sea level and exhibit high sedimentation rates, thus possessing the requisites for an accurate assessment of sea-level change. The early Paleogene epicontinental Tarim seaway, connected with the Tethyan Ocean in a relative tranquil tectonic setting (Tang et al., 1992; Bosboom et al., 2014; Zhang et al., 2018; Li et al., 2021b), is excellently suited at this regard.

2. Geological setting

2.1. Regional geology

The Tarim Basin is the largest inland basin of China, covering an area of 530,000 km^2 bounded by the Tianshan Range on the north, the West Kunlun Range on the south, the Pamir Plateau on the west-southwest, and the vast Taklimakan Desert on the east (Fig. 1A). The Tarim seaway formed during the early Late Cretaceous (Cenomanian), when Tethyan sea waters first encroached eastward through the narrow depression between the Tianshan and Kunlun Ranges. The Tarim Sea experienced five major transgressions until the end of the Paleogene (Tang et al., 1992; Bosboom et al., 2011, 2014; Sun and Jiang, 2013; Sun et al., 2016; Zhang et al., 2018; Kaya et al., 2019). Transgressive-regressive cycles induced by climatic or tectonic events played a major role in the paleogeography and paleoclimate history of central Asia (Hao and Zeng, 1984; Zhang et al., 2018; Kaya et al., 2019). Paleocene-Eocene strata were deposited during the third transgression of the Tarim Sea and are widely exposed in the southwestern Tarim Basin (Zhang et al., 2018; Xi et al., 2020; Li et al., 2021b). This excellently preserved sedimentary record provides a complete archive of eastern Tethyan paleoceanic and paleoclimatic events.

2.2. Lithostratigraphy and biostratigraphy

Two stratigraphic sections with continuous exposure of Cretaceous to Neogene strata were measured at Kuzigongsu (39°44′19″N, 75°18′20″E) and Bashibulake (39°51′18″N, 74°32′44″E; Fig. 1B-C) in the Wuqia County (Xinjiang Uygur Autonomous Region, NW China). The upper Paleocene/lower Eocene Qimugen Formation conformably overlies the Aertashi Formation (Fig. 2D), consisting of thick gypsum and anhydrite with intercalated dolomitic limestone. The lower member of the Qimugen Formation is mostly made of grey-green limestone and marlstone, whereas the upper member chiefly consists of purple-red gypsiferous argillite. The overlying Kalataer Formation is

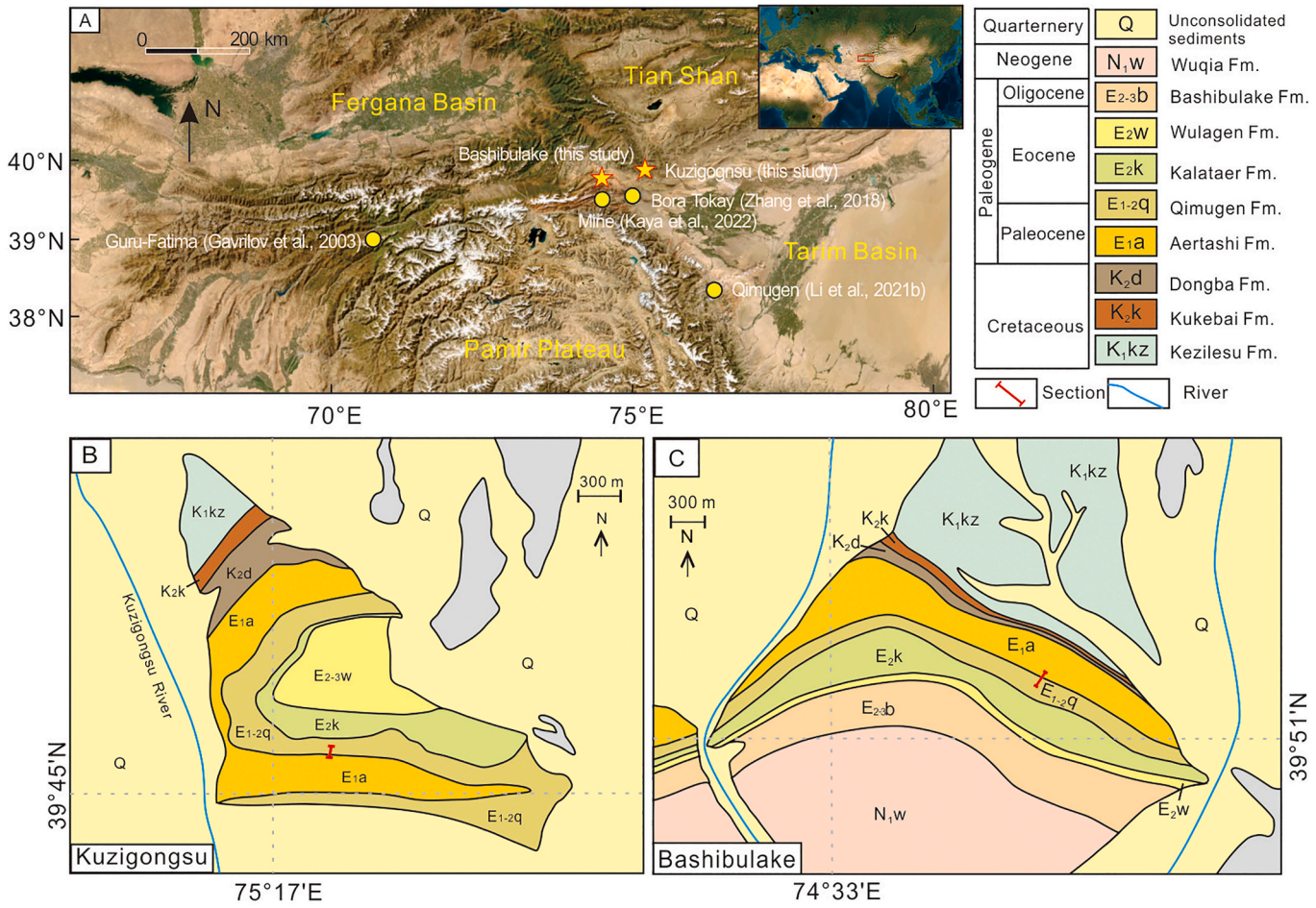

Fig. 1. Topographic and geological maps. (A) Topographic map of the study area and adjacent region with major tectonic units; (B—C) Geological map of Kuzigongsu and Bashibulake study areas, modified from Zhang et al. (2018).

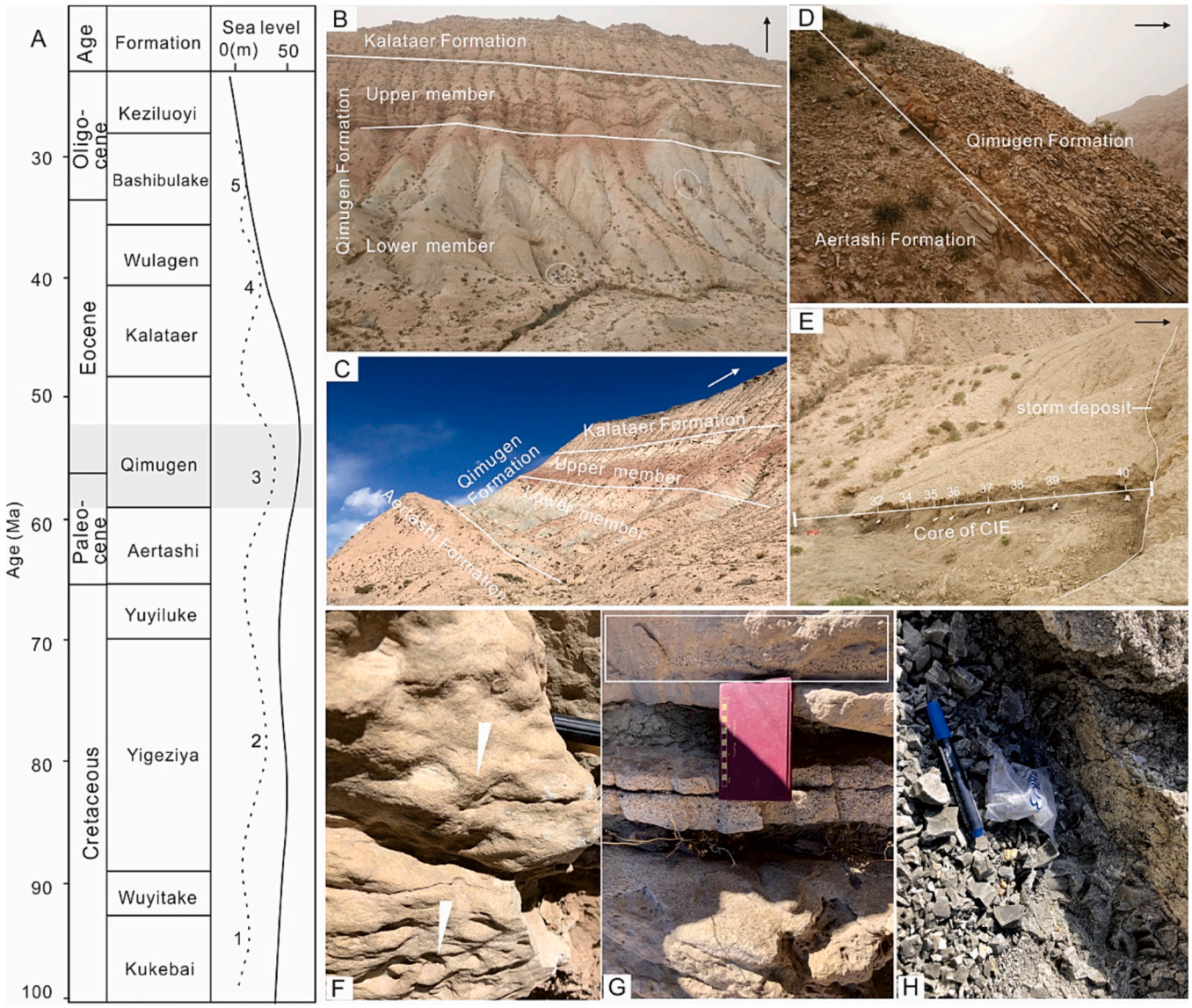

Fig. 2. (A) Regional stratigraphy and Late Cretaceous to Paleogene sea-level curve for the Tarim Basin (Bosboom et al., 2014). Field photos of Kuzigongsu (B) and Bashibulake (C) sections. (D) Boundary between Aertashi and Qimugen formations. (E) Stratigraphic range of CIE core showing sample positions (white line represents erosive surface at base of storm deposit). (F) Interference ripple marks (white arrows) in lower member of Qimugen Formation. (G) Sandy tidal channel deposits and modified "mud-covered sand" structure (rectangle above the notebook). (H) Onset-PETM strata in Bashibulake section. Arrows point up-section.

characterized by the abundance of oyster beds (Tang et al., 1989; Zhang et al., 2018). Based on previous work (Cao et al., 2018; Jiang et al., 2018; Wang et al., 2022a, 2022b, 2023), the present study focuses on the lower member of the Qimugen Formation that contains the PETM event.

Abundant calcareous nannofossils, planktonic foraminifera and dinoflagellates indicate a late Paleocene to early Eocene age for the lower member of the Qimugen Formation (Cao et al., 2018; Jiang et al., 2018). The detailed sedimentological study of the Qimugen section by Li et al., (2021b) documented transgression and storm intensification through the PETM and ETM2 hyperthermal events. Based on high-resolution calcareous-nannofossil biostratigraphy of the Kuzigongsu section, Wang et al., (2022a) inferred a productivity increase during the PETM compensated by a decreased preservation of fossil tests due to acidification. The calcareous-nannofossil study of both Kuzigongsu and Bashibulake sections allowed Wang et al. (2023) to evaluate sea-level changes during the PETM.

3. Methods

Stratigraphic logs of ~47 m and > 80 m were measured in the Kuzigongsu (Fig. 2B) and Bashibulake (Fig. 2C) sections, respectively. Overall, 80 and 76 marlstone and limestone samples were collected for microfacies and carbon-isotope analysis, with a frequency of ~0.5 m (Kuzigongsu) and ~ 1 m (Bashibulake).

3.1. Microfacies analysis

Microfacies analysis was based on sedimentary structures observed in the field and on fossil assemblages, grain composition, and textures identified in thin section. Limestones (siliciclastic detritus <10%) and mixed carbonate-siliciclastic rocks (siliciclastic detritus >10%) were described following Dunham (1962); (integrated by Embry and Klovan, 1971) and Mount (1985), respectively. Environmental interpretation was based on the standard microfacies and depositional model of Flügel (2010). Relative abundances of different allochems (e.g., planktonic foraminifera) were estimated optically under the microscope considering at least 5 fields of view.

3.2. Stable carbon and oxygen isotopes

Powdered samples were obtained by micro-drilling, taking care to avoid veins, pores, and macrofossils. Isotope ratios were measured at the State Key Laboratory for Mineral Deposits Research, Nanjing University, using a Finnigan MAT Delta Plus XP mass spectrometer coupled with an in-line GasBench II autosampler. Samples were reacted with purified orthophosphoric acid at 70 °C. Isotopic measurements were calibrated to the Chinese national standard calcium carbonate sample GBW04405 ($\delta^{13}C_{VPDB}$ = 0.57 ± 0.03‰; $\delta^{18}O_{VPDB}$ = 8.49 ± 0.14‰). Data are expressed in standard delta notation (δ), as permil deviations from the Vienna Pee Dee Belemnite (VPDB) standard. Duplicate measurements of standards yielded an average analytical precision (1σ) of 0.03‰ for $\delta^{13}C$ and of 0.04‰ for $\delta^{18}O$. The complete dataset is provided in Table S2–3.

4. Microfacies analysis and sedimentary evolution

Eleven microfacies (MF) are identified in the lower member and base of the upper member of the Qimugen Formation; representative microfacies are shown in Fig. 3 and simplified microfacies descriptions are given in Table 1.

4.1. Outer ramp environments

4.1.1. MF1 Wackestone

MF1 consists of greyish-green marlstone in the middle and upper parts of the lower member of the Qimugen Formation. Carbonate grains (15–25%) are mainly planktonic foraminifera and filaments. Small benthic foraminifera, calcospherites, serpulids, and crinoids also occur. Matrix is mainly micrite with 0–15% terrigenous clay (Fig. 3A).

MF1 corresponds to standard microfacies 3 of Flügel (2010). The faunal assemblage and micrite indicate a low-energy outer-ramp environment below storm wave base (Fig. 6).

4.1.2. MF2 Bioclastic wackestone/packstone

MF2 consists of greyish-green, thick-bedded bioclastic limestone

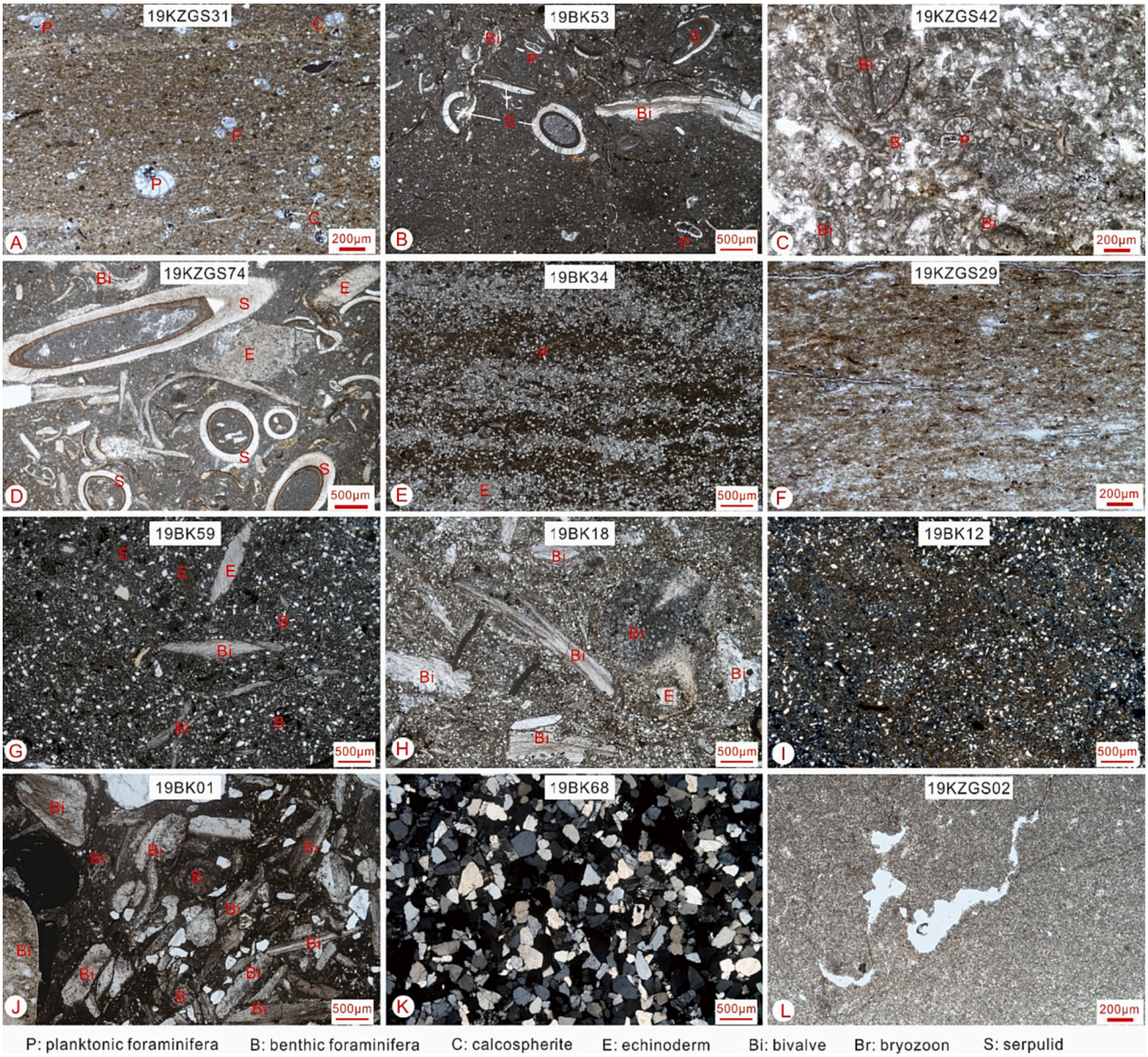

Fig. 3. Thin-section photographs of representative microfacies from Kuzigongsu and Bashibulake sections: (A) MF1 wackestone; (B—C) MF2 bioclastic wackestone/packstone; (D) MF3 (sandy) bioclastic wackestone; (E) MF4 sandy mudstone/wackestone; (F) MF5 mudstone; (G) MF6 sandy mudstone; (H) MF7 (sandy) bioclastic wackestone; (I) MF8 sandy mudstone; (J) MF9 (sandy) wackestone/floatstone; (K) MF10 (micritic) sandstone; (L) MF11 dolomitic mudstone.

Table 1
Average composition, grain size, corresponding standard microfacies, and inferred depositional environment for each microfacies identified in the Kuzigongsu and Bashibulake sections (Qimugen Formation, Tarim Basin).

Microfacies		KZGS section	BSBLK section	Carbonate grains (%)								Groundmass (%)		Terrigenous grains		Standard microfacies (Flügel, 2010)	Depositional environment
				G	Bi	Cr	Co	BF	Br	Se	Os	F	PF	Matrix	Cement	Content (%)	Size range (mm)		
MF1	Wackestone	Y	Y	–	1	1	–	2–6	–	2	–	5–10	4–10	75–85	–	–	–	SMF3	Outer ramp
MF2	Bioclastic wackestone/packstone	Y	Y	–	10–25	3	1	2–5	2	10–15	1	10–15	10–20	45–55	–	0–5	0.05	SMF12-S	Middle-Outer ramp
MF3	(Sandy) bioclastic wackestone	Y	Y	–	2	1	–	1	1	5–10	1	2–5	2–5	65–85	–	5–20	0.05–0.1	SMF8	Middle ramp
MF4	Sandy mudstone/wackestone	Y	Y	–	0–5	1	–	1	1	2–5	–	0–5	0–5	45–80	–	15–50	0.05–0.25		Middle ramp
MF5	Mudstone	Y	Y	–	1	–	–	–	–	–	–	–	2–5	95–100	–	0–5	0.05		Middle ramp
MF6	(Sandy) mudstone	N	Y	–	2–5	2–5	–	–	–	–	–	–	–	85–95	–	5–17	0.1–1.0		Open marine
MF7	(Sandy) bioclastic wackestone	N	Y	–	5–15	5–8	1	0–1	5–10	2–5	–	1	1	70–85	–	5–20	0.02–0.07		Open marine
MF8	Sandy mudstone/micritic Sandstone	Y	Y	–	2–3	–	–	1	–	1–10	1–2	–	–	30–90	–	10–70	0.02–0.15		Open marine
MF9	(Sandy) wackestone/floatstone	Y	Y	1	5–20	5–10	2	2	3	–	–	–	–	55–80	–	0–15	0.2–2	SMF24	Subtidal to lagoon
MF10	(Micritic) sandstone/sandy mudstone	Y	Y	–	–	–	–	–	–	–	–	–	–	–	0–15	85–100	0.1–0.6		Intertidal zone
MF11	(Dolomitic) mudstone	Y	Y	1	–	–	–	1	–	–	1	–	–	95–97	–	–	–	SMF23	Supratidal zone

G: Gastropod; Bi: Bivalves; Cr: Crinoids; Co: Coralline algae; BF: Benthic foraminifera; Br: Bryozoans; Se: Serpulids; Os: Ostracods; F: Filaments; PF: Planktonic foraminifera; KZGS: Kuzigongsu; BSBLK: Bashibulake.

commonly intercalated with MF1 in the middle or upper parts of the lower member of the Qimugen Formation. Carbonate grains (45–55%) are dominated by oysters (*Turkostres*) commonly larger than 2 mm, associated with planktonic foraminifera, filaments, serpulids, crinoids, bryozoans, ostracods, and small benthic foraminifera. Matrix is micrite with minor terrigenous silt (Fig. 3B-C).

MF2 corresponds to standard microfacies 12-S of Flügel (2010). Although oysters, which are widespread throughout the western Tarim Basin (Zhang et al., 2018), generally thrive in warm shallow seas (Lan and Wei, 1995), the abundance of background micrite, planktonic foraminifera and filaments point to a deeper-water depositional environment (Van der Zwaan et al., 1990). The sharp basal contacts of MF2 with MF1 observed in outcrop indicate storm events on an outer-ramp (Fig. 2E, 6). These storm-induced shell layers were quite commonly deposited in the Tarim Sea during this period, suggesting storm intensification (Fig. S2).

4.2. Middle ramp environments

4.2.1. MF3 (Sandy) bioclastic wackestone

MF3 consists of greyish-green marlstone and thick-bedded bioclastic limestone in the upper part of the lower member of the Qimugen Formation. Carbonate grains (15–35%) are mainly filaments, echinoderms, and serpulids. Bivalves, ostracods, bryozoans, benthic and planktonic foraminifera also occur. Matrix is mainly micrite (Fig. 3D).

The high faunal diversity indicates an open environment. Serpulids mainly live today in restricted coastal environments at water depths <30 m (Fornos et al., 1997), but in older times they also lived in deeper waters. MF3 serpulids are relatively complete and set in background micrite together with complete echinoderm tests, filaments and planktonic foraminifera, thus pointing to in situ deposition on a middle to outer-ramp, at water depth ≥ 20 m (Scholle and Ulmer-Scholle, 2003; Flügel, 2010; Fig. 6).

4.2.2. MF4 Sandy mudstone/wackestone

MF4 consists of greyish-green marlstone in the middle to upper parts of the lower member of the Qimugen Formation. Grains are mainly quartz (10–20%) and bioclasts (5–10%), including bivalves, planktonic foraminifera, ostracods, echinoderms, serpulids, and a few small benthic foraminifera. Matrix consists of micrite and quartzose silt (Fig. 3E).

High biodiversity indicates an open environment where angular to subangular terrigenous quartz and broken bioclasts were transported by waves. Micrite and planktonic foraminifera indicate deposition on a middle to outer-ramp (Fig. 6).

4.2.3. MF5 Mudstone

MF5 occurs in the middle part of the lower member of the Qimugen Formation. Sporadic grains include planktonic foraminifera and bivalves set in micrite with quartzose silt locally (Fig. 3F).

MF5 mudstones indicate a low-energy environment below the euphotic zone, possibly a middle-ramp below fair-weather wave base (Fig. 6).

4.3. Open marine environments

4.3.1. MF6 (Sandy) mudstone

MF6 consists of purple-red limestone at the base of the upper member of the Qimugen Formation. Sparse grains 0.1–1 mm in size are bivalves (2–5%), crinoids (2–5%), and terrigenous quartz (5–17%) set in micritic matrix containing quartzose silt (Fig. 3G).

Dominant mud and lack of pelagic fauna suggests a low-energy, open-marine, inner ramp environment below fair-weather wave base (Fig. 6).

4.3.2. MF7 (Sandy) bioclastic wackestone

MF7 consists of greyish-green limestone in the middle part of the

lower member of the Qimugen Formation. Grains include terrigenous quartz (5–20%) and diverse bioclasts (20–40%) including bivalves (5–15%), bryozoans (5–10%), crinoids (5–8%), a few serpulids, and minor planktonic and benthic foraminifera, filaments, and coralline algae set in micritic matrix (Fig. 3H).

High biodiversity of commonly broken shallow-marine bioclasts points to deposition on a relatively high-energy, open marine, inner-ramp above fair-weather wave base (Fig. 6).

4.3.3. MF8 Sandy mudstone/micritic sandstone

MF8 consists of greyish-green to greyish marlstone or calcareous sandstone in the middle part of the lower member of the Qimugen Formation. Detrital quartz in variable amounts (10–70%) is associated with a few serpulids, bivalves, ostracods, and glaucony. Clasts range between 0.02 and 0.15 mm in size. Matrix is mixed micrite and terrigenous clay (Fig. 3I).

Abundant detrital quartz and shallow-marine faunas were transported to a relatively open depositional environment from a nearby land or tidal flat (Fig. 6). Glaucony grains suggests reduced sediment supply at the beginning of a transgression (Garzanti, 1991; Bansal et al., 2017).

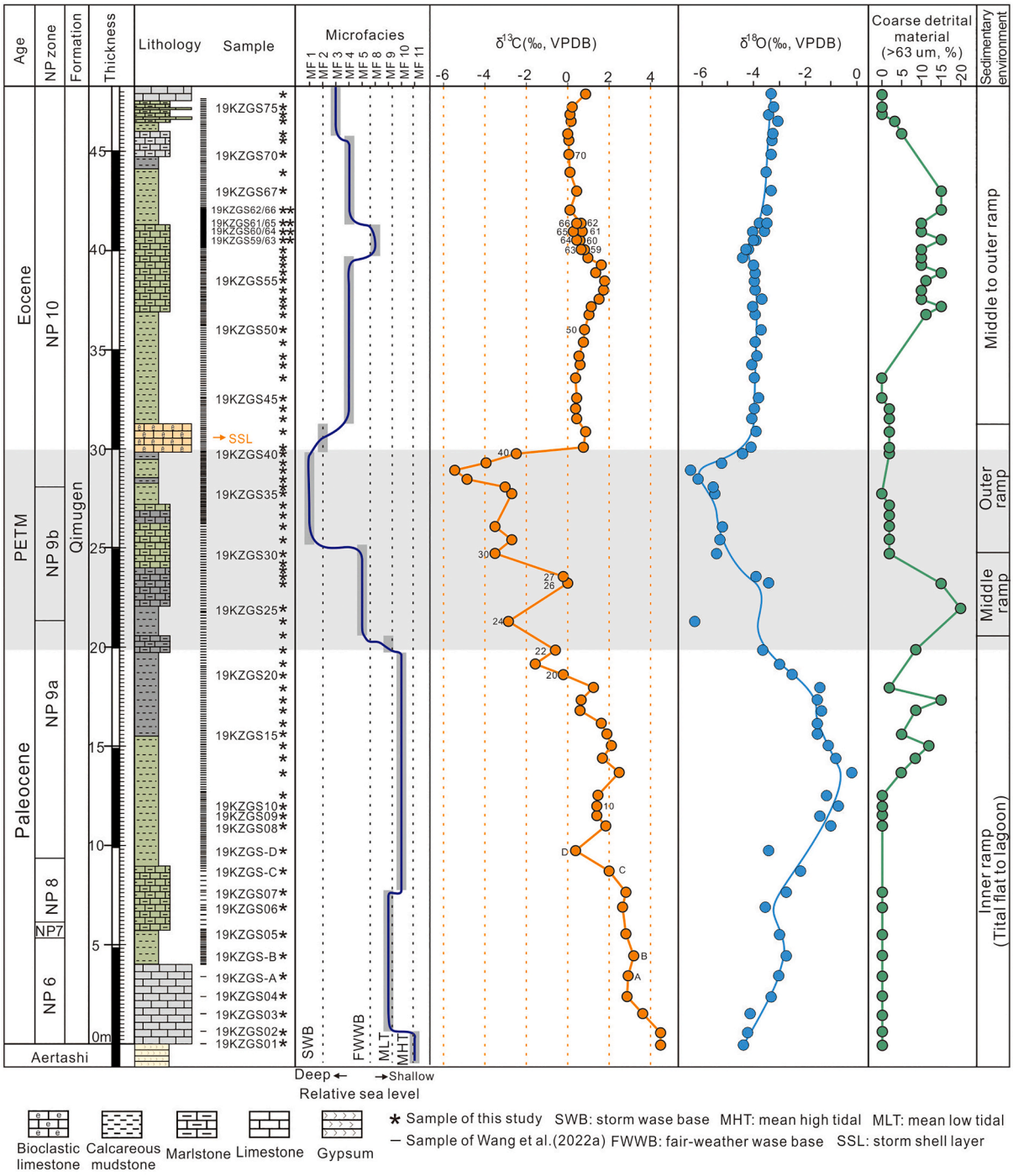

Fig. 4. Stratigraphic log of Qimugen Formation in Kuzigongsu Section, showing microfacies, relative sea level, inferred depositional environment, whole-rock carbonate $\delta^{13}C$ and $\delta^{18}O$ curve, coarse detritus, and calcareous nannofossil zones (NP) after Wang et al. (2022a). VPDB: Vienna Pee Dee Belemnite.

4.4. Lagoonal to tidal flat environments

4.4.1. MF9 (Sandy) wackestone/floatstone

MF9 consists of greyish-green marlstone in the lower part of the lower member of the Qimugen Formation. Detrital quartz with fragments of mudrock and chert (0–15%) occur with common bioclasts (10–35%) including bivalves, crinoids, and a few bryozoans, coralline algae, and small benthic foraminifera. Clasts mainly range between 0.2

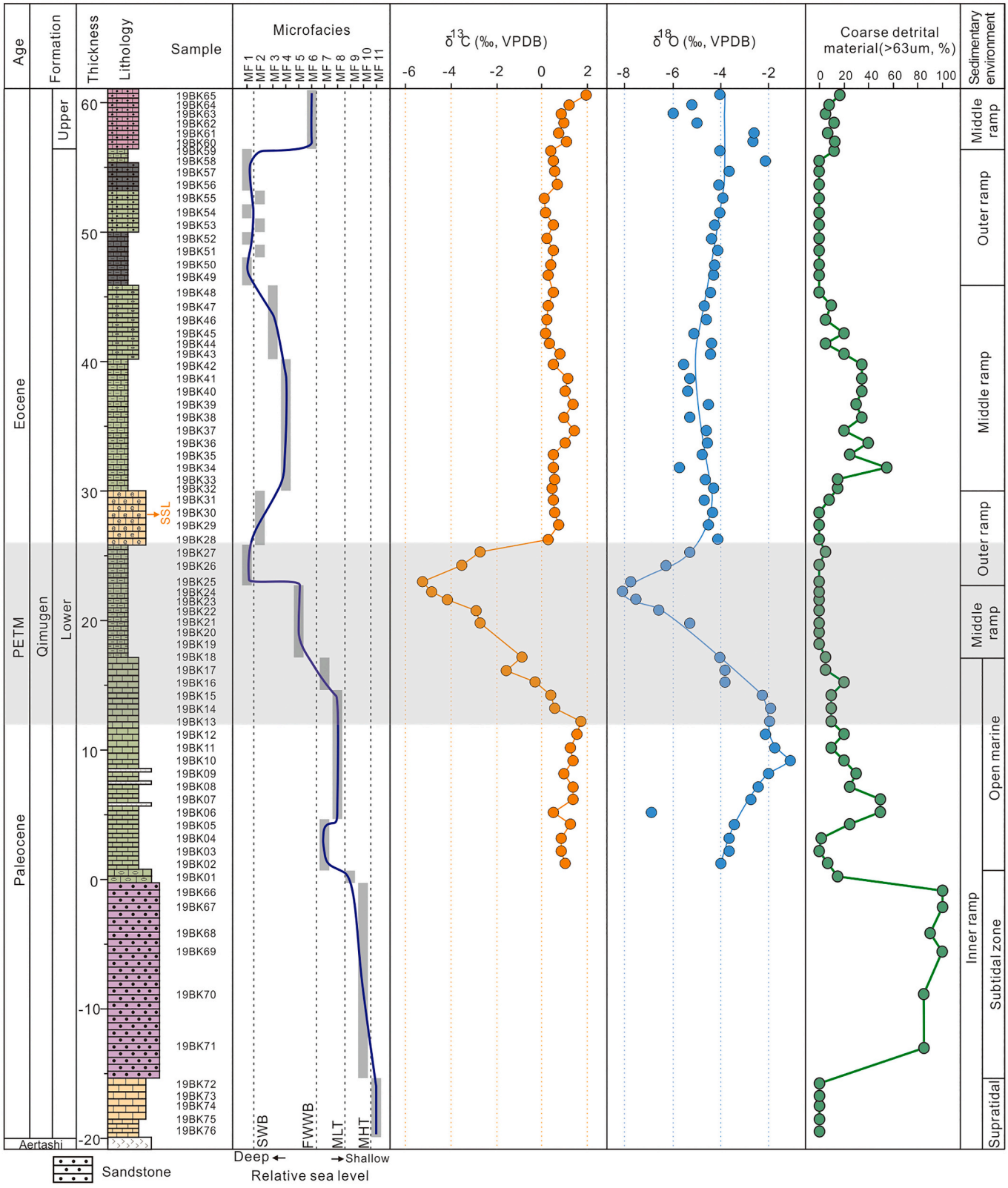

Fig. 5. Stratigraphic log of Qimugen Formation in Bashibulake Section, showing microfacies, relative sea level, inferred depositional environment, whole-rock carbonate $\delta^{13}C$ and $\delta^{18}O$ curve, and coarse detritus. Legend as in Fig. 4.

and 1.5 mm but are locally >2 mm. Matrix is mixed micrite and terrigenous clay. Bioturbation is common (Fig. 3J).

The fossil assemblage and common bioturbation point to a relatively enclosed inner neritic subtidal environment adjacent to a lagoon (Fig. 6).

4.4.2. MF10 (Micritic) sandstone/sandy mudstone

MF10 mainly consists of purple-red or greenish sandstone or calcareous mudstone in the lower part of the lower member of the Qimugen Formation. Sand lenses locally showing erosive base wavy bedding, and interference ripples are embedded in silt or mud (Fig. 2F-G). Detrital quartz (85–100%) is locally associated with bivalves and small benthic foraminifera. Matrix is mixed micrite and quartzose silt. Fine lamination is common (Fig. 3K).

MF10 contains less fossils than the interbedded MF9 and more detrital quartz reworked by tidal currents; erosive structures indicate a tidal channel (Fig. 6).

4.4.3. MF11 (Dolomitic) mudstone

Grey, thin-bedded dolomitic limestone at the base of the Qimugen Formation overlies gypsum of the Aertashi Formation. Micrite or microcrystalline dolomite with *bird's eyes* include a few miliolids, gastropods, and ostracods (Fig. 3L).

MF11, corresponding to SMF23 of Flügel (2010), points to a supratidal environment in arid to semi-arid climate (Scholle et al., 1983).

5. Isotope stratigraphy

The whole-rock inorganic-carbon isotopic curve for the lower member of the Qimugen Formation shows well-defined similar trends in both Kuzigongsu and Bashibulake sections. A clear negative carbon-isotope excursion (CIE) is documented in the middle part of the lower member of the Qimugen Formation, with some differences in the amplitude and fine structure of $\delta^{13}C$ values (Figs. 4 and 5). Our results are consistent with the ultrahigh-resolution (10–20 cm) carbon-isotope stratigraphy and calcareous-nannofossil biostratigraphy of Wang et al. (2022a) (Fig. 7 and S1).

In the lower part of the Kuzigongsu section, $\delta^{13}C$ values range from −0.5‰ to 4.5‰; the CIE begins at 19.9 m above the base of the Qimugen Formation and terminates at 30.5 m, with a most negative $\delta^{13}C$ value of −5.4‰ and a negative-excursion amplitude of 6.7‰. Above the CIE, $\delta^{13}C$ values recover to between 0.0 and − 1.9‰. Carbonate rocks are lacking at the base of the Bashibulake section, and $\delta^{13}C$ values range from 0.5 to 1.7‰ between 1 and 12 m from the base of the Qimugen Formation. The CIE occurs between 12 and 28 m, with a negative-excursion amplitude of 7.0‰. Above the CIE, $\delta^{13}C$ ranges between 0.1 and 2.0‰.

The $\delta^{18}O$ values are between −6.4‰ to −0.2‰ in the Kuzigongsu section, showing a negative excursion with an amplitude of 6.3‰ in the CIE interval. Throughout the Bashibulake section, $\delta^{18}O$ ranges between −8.1‰ and − 1.1‰, showing a negative excursion with an amplitude of 6.2‰ in the CIE interval.

6. Discussion

6.1. The PETM record in the Tarim Basin

The inconspicuous correlation between $\delta^{13}C$ and $\delta^{18}O$ (Fig. 7) indicates that stable isotopes in the Qimugen Formation preserve the original oceanic signal (Banner and Hanson, 1990; Knauth and Kennedy, 2009), with negligible effect of terrigenous supply or diagenesis (in line with Wang et al., 2022a).

The PETM event is defined by the negative carbon-isotope excursion documented in the sedimentary record, the onset of which was conventionally assumed as the Paleocene/Eocene boundary by the International Commission on Stratigraphy (Aubry et al., 2007). In the Kuzigongsu section, the CIE is testified by a 10.6-m-thick interval and includes small-scale excursions, possibly explained by multiple releases of light carbon (Barnet et al., 2019; D'Onofrio et al., 2020). In the Bashibulake section, the CIE is testified by the 16-m-thick interval where $\delta^{13}C$ and $\delta^{18}O$ reach the most negative values of respectively −4.9‰ and − 8.1‰ at ~23 m from the base of the Qimugen Formation. The two sections are robustly correlated by a shell layer (MF2 of this study; sandy limestone layer of Cao et al., 2018 and Jiang et al., 2018) identified throughout the Tarim Basin. The CIE record of the Qimugen Formation (Figs. 4 and 5), similar as that of the Tethys Himalayan carbonate platform (Li et al., 2017, 2020, 2021a) and New Jersey shelfal strata (Self-Trail et al., 2012), shows a more rapid recovery than the typical PETM carbon-isotope structure (McInerney and Wing, 2011). This may be explained by several processes, including fast carbon sequestration driven by increased C-storage in the terrestrial biosphere (Bowen and Zachos, 2010), increased marine export (Torfstein et al., 2010), enhanced silicate weathering (Kelly et al., 2010), decreased sedimentation rate during transgression (Figs. 4 and 5), or erosion because of enhanced storm activity in the recovery stage (Fig. 2E).

6.2. Sedimentary evolution across the PETM

Microfacies analysis indicates that the lower member of the Qimugen Formation documented a complete transgressive-regressive cycle in both Kuzigongsu (Fig. 4) and Bashibulake (Fig. 5) sections (Zhang et al., 2018; Li et al., 2021b). Gypsum layers deposited in sabkha environments at the top of the Aertashi Formation are overlain by supratidal dolomitic mudstones (MF11) at the base of Qimugen Formation. Above, sandstone and floatstone (MF10) exposed in the Bashibulake section were deposited in intertidal to subtidal environments, whereas wackestone and

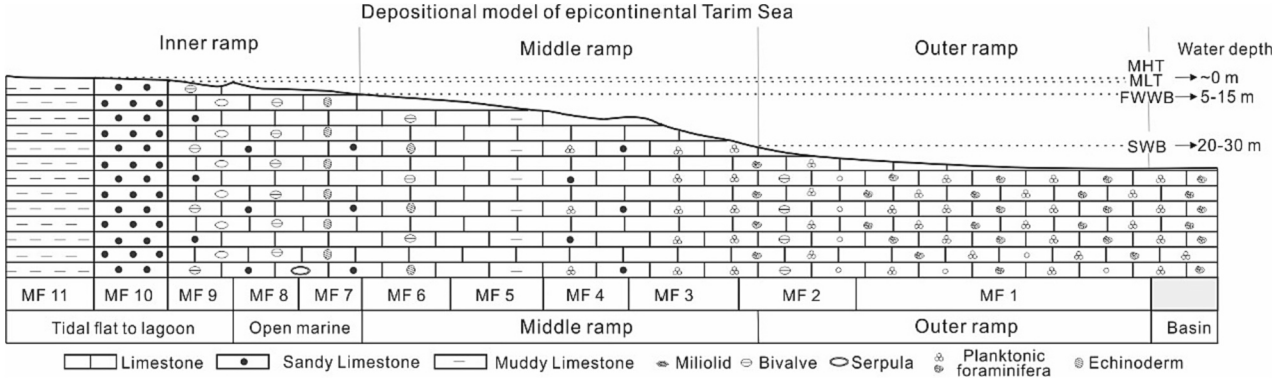

Fig. 6. Depositional model for western Tarim Basin margin in the late Paleocene to early Eocene, with inferred paleo-water depth and position of each identified microfacies.

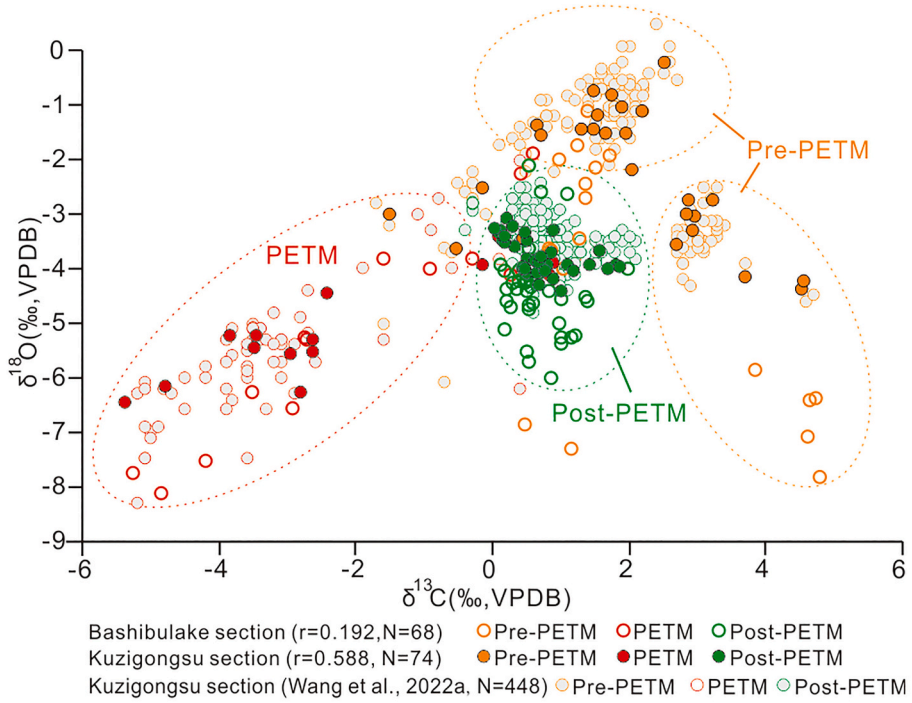

Fig. 7. Cross-plot of whole-rock carbonate carbon isotope versus oxygen isotope values for Qimugen Formation exposed in Kuzigongsu and Bashibulake sections. Grey filled circles represent data of Wang et al. (2022a).

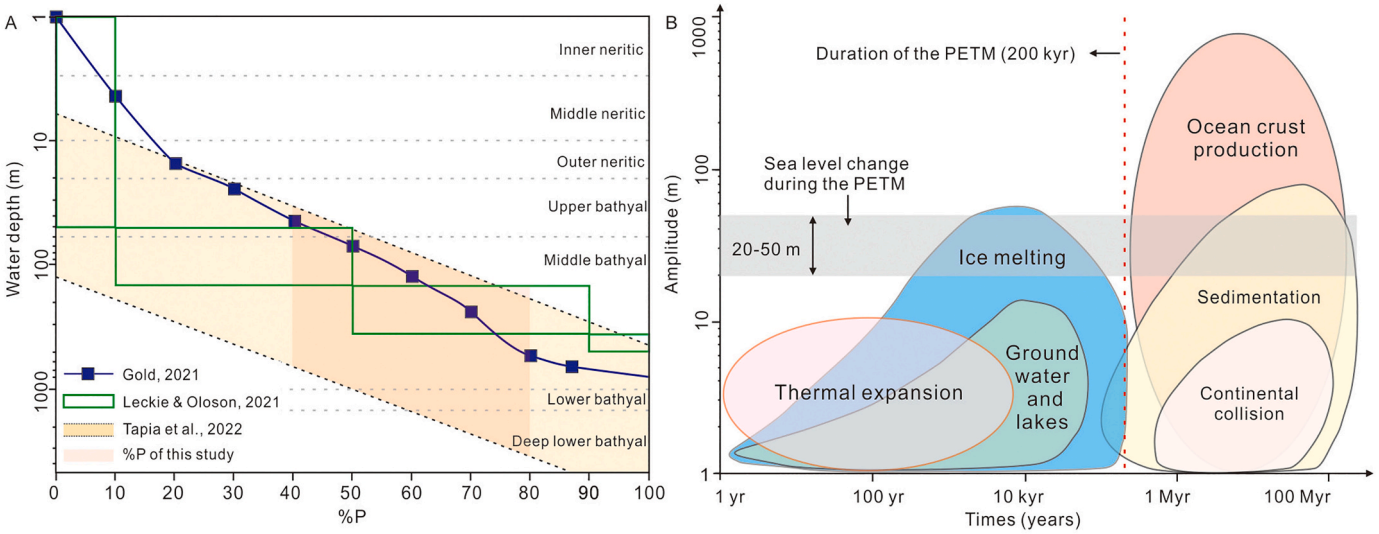

Fig. 8. (A) Graph indicating expected percentage of planktonic foraminifera to total foraminifera with increasing water depth. B) Timing and amplitude of geological controls of eustatic change (mod. From Miller et al., 2005a; Sames et al., 2016).

mudstone with fine lamination (MF9–10) exposed in the Kuzigongsu section accumulated in subtidal to lagoonal environments. Transgression began after this period of relatively constant water depth and depositional conditions. In the Bashibulake section, bioclastic wackestone with abundant shallow marine fossils (MF7–8) indicate transition to an open-marine inner ramp, followed by mudstone with planktonic foraminifera (MF5) deposited on a middle ramp. In the Kuzigongsu section, instead, transgression led directly to deposition of MF5 on a middle ramp, followed by wackestone with planktonic foraminifera and filaments (MF1) interbedded with frequent storm layers with mixed shallow-water and deep-water fossils deposited on an outer ramp (MF2). This interval is inferred to represent a high-stand systems tract documented throughout the basin, followed by a relative stable stage characterized by increasing terrigenous supply and deposition of sandy bioclastic wackestone (MF3) and sandy mudstone/wackestone with planktonic foraminifera and filaments on a middle to outer ramp (MF4). Eventually, sandy mudstone with bivalves and echinoderms (MF6) at the base of the upper member of the Qimugen Formation indicate deposition on an inner to middle ramp during regression.

Microfacies analysis combined with carbon-isotope stratigraphy allows us to accurately reconstruct the sedimentary evolution during the PETM event. Tidal to lagoonal environments influenced by terrigenous supply before the PETM passed upward to open marine to middle-ramp settings at the beginning of the CIE, and later on to outer-ramp settings during the main body of the CIE, returning to middle/outer ramp during the recovery stage until inner/middle ramp deposition influenced by

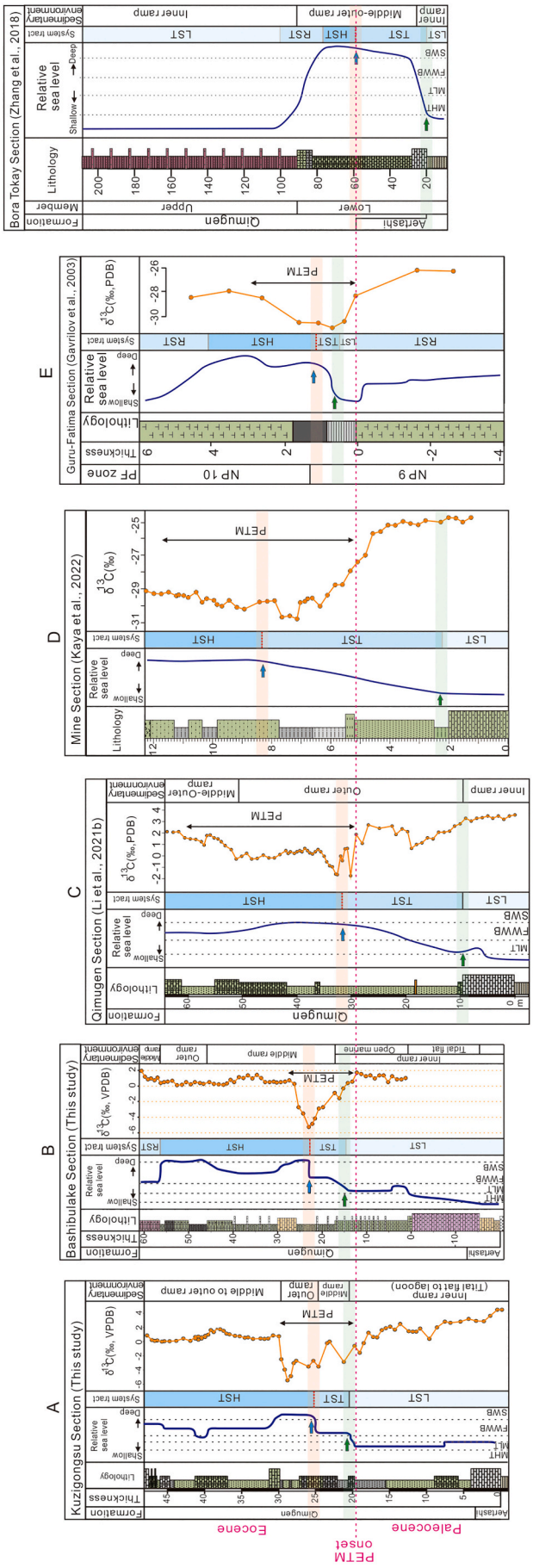

Fig. 9. Compilation of Paleocene-Eocene logs across the Tarim Basin, showing lithology, carbon-isotope stratigraphy, sea-level change and systems tracts (LST: lowstand; TST: transgressive; HST: highstand; RST: regressive). Light green and orange bands indicate transgression initiation and maximum-flooding surface. (For interpretation of the references to colour in this figure legend, the reader is referred to the web version of this article.)

terrigenous material was eventually re-established after the PETM.

6.3. Sea-level change in the Tarim Basin during the PETM

High-resolution microfacies analysis of the Kuzigongsu and Bashibulake sections consistently indicate that the PETM event corresponded to a transgression of the Tarim Sea, reaching maximum flooding at the peak of the PETM (Figs. 4 and 5). Such a deepening event represents the third transgression of the Tarim Sea since the mid-Cretaceous (Tang et al., 1992; Bosboom et al., 2014; Zhang et al., 2018). The reconstructed relative-sea-level curve shows that paleo-water depths fluctuated between mean high tide and mean low tide (i.e., around 0 m) before the PETM and dropped below storm wave base during the PETM. Storm wave base (i.e., the maximum sea-floor depth affected by storms) ranges widely from an average depth of 20–30 m in epicontinental seas to >100 m for open shelves, depending on shelf configuration, shelf-edge topography, climatic zone, and storm intensity (Flügel, 2010; Peters and Loss, 2012). The Tarim Sea was an epicontinental sea, which allows us to grossly infer that storm wave base lay around 20–30 m during the early Paleogene (Tang et al., 1992; Bosboom et al., 2011; Zhang et al., 2018; Li et al., 2021b). The studied strata during the PETM were thus deposited at water depths ≥20–30 m.

Fossil assemblages and the life mode and morphology of organisms provide useful elements to constrain paleo-water depth estimates (Gold, 2021). The percentage of planktonic foraminifera to total rock and the ratio of planktonic to total foraminifera [**%P** = P/(P + B), where P and B are frequencies of planktonic and benthic foraminifera] are most sensitive to changes in sea level, especially in mixed siliciclastic-carbonate environments as those of the Tarim Basin (Leckie and Olson, 2003; Tapia et al., 2022). Excepting MF2 storm layers, the percentage of planktonic and benthic foraminifera in the Qimugen Formation were 4–10% and 2–6% (Table 1), and therefore the %P lies in the 40–80% range, pointing to a maximum paleo-water depth either between 50 m and ≥ 200 m (Leckie and Olson, 2003; Gold, 2021) or between 32 m and 108 m (if calculated by the regression formula, Depth = $2^{(3.365+(0.0407*\%P))}$ of Tapia et al., 2022). These estimates are obviously tentative and rough, because planktonic foraminifera do feed in the photic zone with highest concentrations between water depths of 10 and 50 m but, after death, their tests may settle through the water column to greater depths or even be entrained by currents towards shallower depths (Bé, 1977; Flügel, 2010; Gold, 2021). Notwithstanding these limitations and the overall low content of foraminifera in the Qimugen Formation, a maximum paleo-water depth constrained by foraminifera indicators during the PETM can be plausibly considered as no <30 m and up to ≥50 (Fig. 8A). This is consistent with MF1-MF4 fossil assemblages characterized by filaments and serpulids (Scholle and Ulmer-Scholle, 2003; Flügel, 2010) and with the abundance of the calcareous nannofossil *Micrantholithus* during the PETM, a *taxon* that mainly lived in middle to outer neritic environments (Wang et al., 2022a; Wang et al., 2023).

Microfacies analysis and foraminiferal indicators help us to conservatively constrain the relative sea-level change documented by the Qimugen Formation during the PETM to between a minimum of 20 m and a maximum ≥50 m. This estimate is compatible with sedimentological evidence from other parts of the Tarim Basin, including the Qimugen (Fig. 9C; Li et al., 2021b) and Mine sections (Fig. 9D; Kaya et al., 2019, 2022). The Tarim seaway thus recorded the same evolution of relative sea level during the PETM, with transgression at, or slight earlier than PETM onset followed by high-stand conditions during the main part of the PETM. Microfacies and biostratigraphy of the Bora Tokay section also testify to a transgression near the Paleocene-Eocene boundary (Fig. 9F; Zhang et al., 2018). The Guru-Fatima section in the western Tarim Basin documents a minor regression before the PETM, possibly related to regional factors (Fig. 9E; Gavrilov et al., 2003), followed by transgression and high-stand conditions during the PETM. The relative sea-level changes observed throughout the Tarim Basin had an impact on ecological and depositional systems, including increased

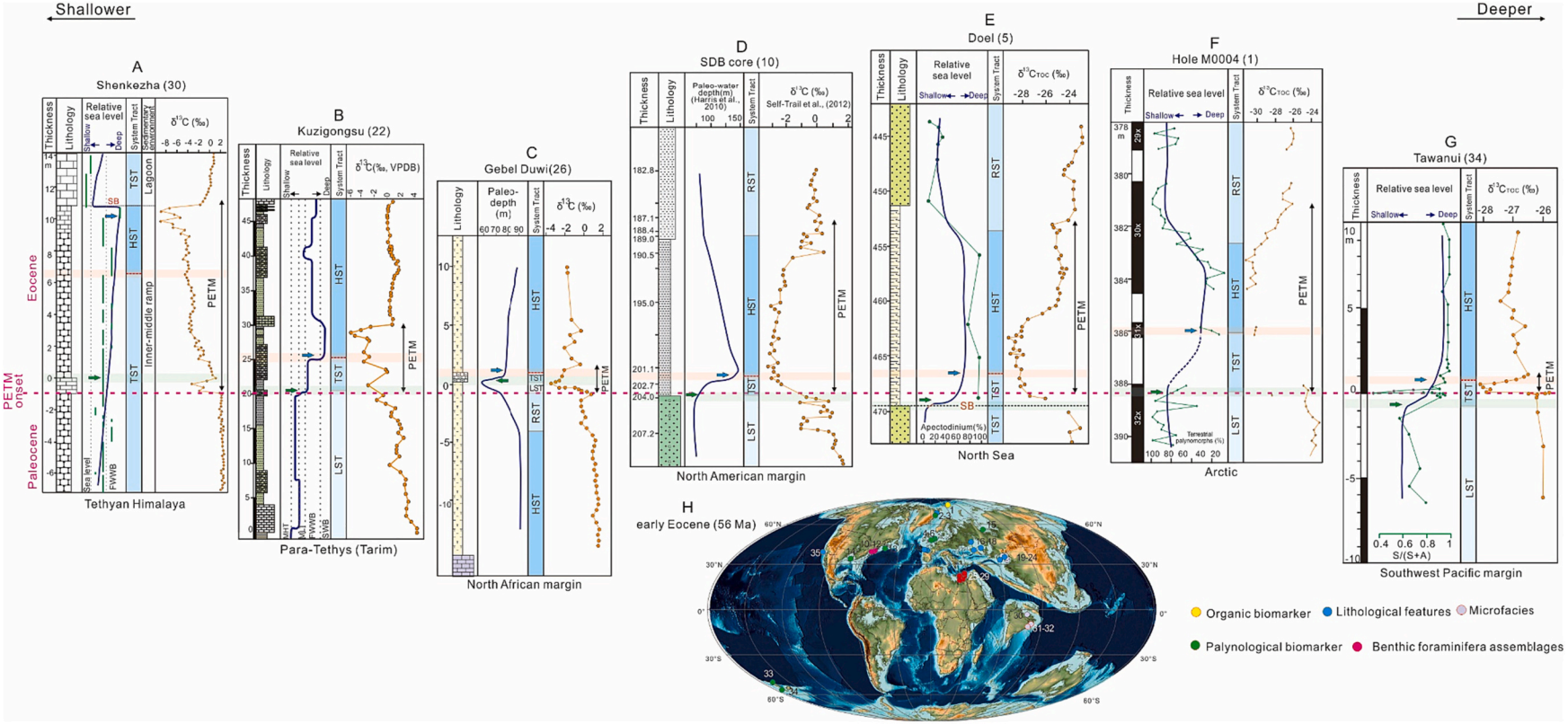

Fig. 10. Compilation of representative Paleocene-Eocene logs worldwide, showing lithology, carbon-isotope stratigraphy, sea-level change, and systems tracts (SB: sequence boundary). Light green and orange bands indicate transgression initiation and maximum-flooding surface. (A) Shenkezha section (Li et al., 2020); (B) Kuzigongsu section (this study); (C) Gebel Duwi section (Speijer and Morsi, 2002); (D) SDB Core (Self-Trail et al., 2012); (E) Doel section (Sluijs et al., 2008); (F) Hole M0004 (Sluijs et al., 2006); (G) Tawanui section (Sluijs et al., 2008); (H) Early Eocene paleogeographic map showing key locations discussed in text (mod. From Scotese, 2021). Colored dots represent different sea-level indicators (see Table S1 for further information). (For interpretation of the references to colour in this figure legend, the reader is referred to the web version of this article.)

deep-water species (*Micrantholithus*) and, enhanced terrigenous input and weathering intensity (Wang et al., 2022a). The size of terrigenous quartz grains tends to decrease during the PETM interval in both Bashibulake and Kuzigongsu sections (Fig. 4-5), which may be also an effect of relative sea-level rise.

The observed sea level rise during the PETM is associated with the third transgression of the Tarim Sea and represent the maximum flooding of this period (Tang et al., 1992; Bosboom et al., 2014; Zhang et al., 2018). However, on a long-term perspective, the transgression started at the end of the sedimentation of the Aertashi Formation and continued for >5 million years (Hao and Zeng, 1984; Tang et al., 1989; Zhang et al., 2018; Kaya et al., 2019; Xi et al., 2020). This transgression has been ascribed to either eustasy or far-field effects of the Indo-Asian collision (Zhang et al., 2018; Kaya et al., 2019). The former hypothesis is here preferred and discussed below. Actually, the rapid sea level rise recorded during the PETM was superimposed onto this long-term transgression, which may account for why the third transgression represented the largest sea level change in the region (Bosboom et al., 2011; Zhang et al., 2018).

6.4. Eustatic change during the PETM

Relative sea-level changes across the PETM have been described from North Africa (Fig. 10C; Speijer and Morsi, 2002; Speijer and Wagner, 2002), southwestern Pacific Ocean (Fig. 10G; Sluijs et al., 2008), North America (Fig. 10D; John et al., 2008; Harris et al., 2010; Self-Trail et al., 2012; Sluijs et al., 2014), North Sea (Fig. 10E; Sluijs et al., 2008), Arctic Ocean (Fig. 10F; Sluijs et al., 2006; Harding et al., 2011), Tethys Himalaya (Fig. 10A; Li et al., 2017, 2020; Sreenivasan et al., 2022), Biscay Bay (Schmitz and Pujalte, 2003; Pujalte et al., 2016), and Para-Tethys (Fig. 9; Gavrilov et al., 2003; Li et al., 2021b; Kaya et al., 2022). Sea-level rise was constrained to between 20 and 30 m based on ostracod assemblages from the North African margin (Speijer and Morsi, 2002) and to between 50 and 100 m based on benthic foraminifera from the North American margin (Harris et al., 2010). Sea-level changes, however, were not recorded everywhere at the same time, also depending on the distance from the coast (Sluijs et al., 2008). In most cases, relative sea-level started to rise before the CIE (e.g., southwestern Pacific: Sluijs et al., 2008; North America: Harris et al., 2010; Arctic Ocean: Sluijs et al., 2006). In other cases, sea-level started to rise at CIE onset and transgressive deposits directly overlie a sequence boundary (North Africa: Speijer and Morsi, 2002; North Sea: Sluijs et al., 2008). In nearly all cases, high-stand conditions where reached during the peak of the PETM, although aggrading siliciclastic sediments were deposited at this stage in the Basque basin of northern Spain (Schmitz and Pujalte, 2003; Pujalte et al., 2016; Li et al., 2021a) or in the Xigaze forearc basin of southern Tibet (Jiang et al., 2021). These units are inferred to document increased terrigenous supply as a response to the enhanced hydrological cycle (Pujalte et al., 2016; Chen et al., 2018; Jiang et al., 2021). During the recovery stage of the PETM and after it, relative sea-level trends varied slightly in different regions. Some areas remained in high-stand conditions (e.g., Tarim Sea, North African and Southwest Pacific margins; Fig. 10) while others documented a mild regression (e.g., North America margin, North Sea and Arctic), which may be related to the recovery of the Earth system (Gaia hypothesis; Lovelock, 1979), and further suggesting that climate effects during the PETM might be the primary factor influencing the sea level change. In all cases, however, sea level remained higher than before the PETM, with the only exception of the Tethys Himalaya where relative sea level dropped rapidly after the recovery stage, plausibly because of incomplete sedimentary record or flexural tectonic uplift during ongoing India-Asia collision (Li et al., 2017, 2020). Besides these local inconsistencies, which are expected considering regional differences in climatic and tectonic regimes and the complexities of feedback systems, worldwide evidence of relative sea-level rise across the PETM can be safely considered to largely reflect global eustasy.

6.5. Mechanisms of eustatic change during the PETM

The causes of global sea-level variations belong to two categories: change in total seawater and change in ocean-basin volume (Miller et al., 2005a; Li et al., 2023). The former category, including glacier melting, thermal expansion, or groundwater and lake changes, controls short-period (< 1 Ma) eustatic change. The latter category, including accelerated sea-floor spreading, continental collision, or increased sedimentation rate, controls slower longer-period eustatic change (Fig. 8B). Sea-level rise during the PETM was rapid, and thus chiefly influenced by changes in the total amount of seawater. Different potential mechanisms are examined below.

6.5.1. Thermal expansion

The Earth's oceans play a crucial role in regulating the surface climate system by absorbing and transporting heat. Seawater volume expands or contracts in response to temperature change, leading to eustatic change (Church et al., 2010). Our understanding of this effect is primarily based on modern observations and simulations, which reveal that the process is nonlinear and influenced by initial temperature, salinity, and pressure of seawater (Wigley and Raper, 1987; Widlansky et al., 2020). Current data indicate that thermal expansion of ocean water causes a eustatic rise of ~1.3 mm/year, accounting for about one-third of the overall increase in sea level (National Oceanic and Atmospheric Administration NOAA, 2023). If we assume such a rate of eustatic change combined with a PETM onset stage of ~6000 years (Li et al., 2023), then thermal expansion would have caused a eustatic rise of ~7.8 m during the PETM. If 1 °C of seawater warming corresponded to a eustatic rise of ~0.7 m (Conrad, 2013; Sames et al., 2016) and global temperature rose by 5–8 °C (Tripati and Elderfield, 2005; Zachos et al., 2006; Tierney et al., 2022), then thermal expansion may have caused a eustatic rise between 3.5 and 5.6 m during the PETM. We conclude that thermal expansion of seawater did contribute significantly but could account for only a subordinate part of eustatic rise during the PETM, estimated in this study to have been of 20 m at least.

6.5.2. Groundwater and lake changes

Continents act as the primary reservoir for removing water from the oceans, with the potential to affect global sea level at the short timescale (Hay and Leslie, 1990). This mechanism, called aquifer eustasy (or sponge-continent hypothesis), operates on the principle that atmospheric precipitation regulates the transport of water from the ocean to the land and is often used to explain sea-level changes during greenhouse periods (Davies et al., 2020; Sames et al., 2016; Li et al., 2018, 2023). Because the change of groundwater and lake level has generally an inverse phase relationship with sea level (Sames et al., 2020; Wang et al., 2020), information on lake-level changes during the PETM is relevant to our goal. The not many reported cases of the PETM in lacustrine environments include the Nanyang (Chen et al., 2014, 2016), Jianghan (Teng et al., 2021; Xie et al., 2022), and Sichuan (Yang et al., 2018) basins in central and western China and the Paris Basin in France (Smith et al., 2011). The lake level of all these basins rose during the PETM. For instance, the Jianghan Basin passed from pelite with thin gypsum layers to clay and silt deposited in a deeper environment (Teng et al., 2021; Xie et al., 2022) and the Paris Basin from marginal-lacustrine calcareous sandstone to open-lacustrine mudstone and clay (Smith et al., 2011). Conversely, lowering of the groundwater table in the Willwood Formation of Wyoming (USA) has been inferred based on the reduced abundance of crayfish burrows and molluscan body fossils (Smith et al., 2009), although this trend may be explained by increasing aridity in the region during the PETM. The rise in lake levels during the PETM would testify to an intensified hydrological cycle (Carmichael et al., 2017), resulting in a greater influx of water in groundwater reservoirs (Jackson et al., 2001). Such a transfer of water from the oceans to the continents would have caused a decrease, rather than an increase, of eustatic level during the PETM.

6.5.3. Ice melting

Because thermal expansion can only explain a fraction of eustatic change during the PETM and aquifer eustasy is ruled out, only ice melting is left as a potential control. But did glaciers of sufficient size exist during the PETM?

Direct evidence of ice melting (e.g., ice raft deposition) is lacking, and only speculations based on indirect indicators or models can be made. Previous studies have suggested that, although greenhouse conditions persisted through the early Paleogene, global temperatures and CO_2 concentration in the atmosphere were decreasing since the end of the Cretaceous and small mountain glaciers could exist in Antarctica (DeConto and Pollard, 2003; Miller et al., 2005b; Li et al., 2022b). Eustatic rise driven by ice melting during the PETM is consistent with a decrease in $\delta^{18}O$ caused by an influx of water enriched in ^{16}O (Rovere et al., 2016; Gold, 2021), as observed in Qimugen carbonates (Figs. 4 and 5). High temperature also leads to a decrease of ^{18}O in precipitation process of calcite by reducing the degree of oxygen-isotope fractionation (Urey, 1947). These considerations lend support to the possibility that glacial melting during the PETM (Sluijs et al., 2008; Harris et al., 2010) was responsible to the main part of eustatic rise (i.e., $\geq$ 12 m, if thermal expansion contributed with another 8 m to reach the inferred total of $\geq$20 m). This would correspond to melting of a glacier volume one-fifth of the modern Antarctic ice-cap (DeConto and Pollard, 2016).

6.5.4. Other mechanisms and feedbacks

Volcanic eruptions and enhanced sea-floor spreading in the North Atlantic region may have contributed to eustatic rise during the PETM, although a magmatic lull indicated to have occurred between two peaks of activity at 62–58 Ma and 55–51 Ma (Saunders et al., 1997; Storey et al., 2007) reduces this possibility. Moreover, simulation studies have failed to suggest significant changes in sea-floor expansion across the PETM (Müller et al., 2016).

The long-term increase of sedimentation rate in the ocean basin will lead to a decrease in ocean volume and hence eustatic rise, but this speculation is difficult to quantitatively constrain during the PETM. Ocean acidification at the onset of the PETM will even reduce the sedimentation rate, thus ruling out the contribution of this mechanism to sea level change in the PETM. As for the continental margin, an intensified hydrological cycle may have resulted in higher sedimentation rates of terrigenous sediments, but this would generally lead to a retreating of shoreline (Carmichael et al., 2018).

In conclusion, we envisage melting of mountain glaciers in Antarctica and thermal expansion of seawater as the most plausible causes of eustatic rise during the PETM. It is crucial, however, to consider also the effect of positive feedbacks on climate, further impacting on ecological and sedimentary systems. For instance, increased seawater temperature and sea-level rise impacted severely on shallow-water ecosystems, which were commonly replaced or destroyed (Sluijs et al., 2014; Sreenivasan et al., 2022). The hydrological cycle was enhanced, resulting in extreme and more frequent storm events (Jiang et al., 2022). Conversely, eustatic rise and flooding of coastal areas (Schulte et al., 2011) may have led to organic-carbon burial, thus promoting recovery and the end of the PETM stage.

7. Conclusions

High-resolution microfacies analysis and carbon-isotope stratigraphy shed light on the latest Paleocene to earliest Eocene sedimentary evolution of the Tarim Basin (Xinjiang Uygur Autonomous Region, NW China). Based on new evidence, we discuss and tentatively constrain the amount and controls of sea-level change recorded during the PETM event.

Microfacies analysis shows that the depositional environment evolved from tidal-flat and lagoon (pre-PETM), to open-marine and middle-ramp (PETM onset), to outer-ramp (*syn*-PETM), and eventually middle- and inner-ramp settings (post-PETM), indicating a gradual transgression that began at PETM onset and led to maximum flooding during PETM peak and recovery. Paleontological (e.g., abundance of planktonic foraminifera) and sedimentological evidence combined indicates that the amplitude of relative sea-level change as recorded by the Qimugen Formation during the PETM was at least 20 m and possibly as much as 50 m.

The correlation of regional and global stratigraphic profiles during the PETM interval suggests that the relative sea-level change recorded by sedimentary strata of the Tarim Basin chiefly represents a global signal. The most plausible drivers of short-term eustatic rise are inferred to have been thermal expansion coupled with melting of significant volume of mountain glaciers in Antarctica (ca. one fifth of the modern ice cap), whereas aquifer eustasy or other mechanisms including enhanced volcanic eruptions and sea-floor spreading in the North Atlantic hardly represent relevant factors. A proper understanding of the PETM event and associated eustatic rise needs to fully consider the complexities associated with feedbacks between climatic, ecological, and sedimentary systems.

Declaration of Competing Interest

The authors declare that they have no known competing financial interests or personal relationships that could have appeared to influence the work reported in this paper.

Data availability

Data will be made available on request.

Acknowledgement

We thank Zhilin Yang, Shijie Zhang, Wei Li, Hong Su, Yangguang Gu, and Caiying Zhong for assistance in the field. This work, supported by the National Natural Science Foundation of China (41888101, 42072117), and by the program B for Outstanding PhD candidate of Nanjing University, is a contribution to the UNESCO IGCP 739. This paper is dedicated to our dear friend and co-author Dr. Juan Li who spent her last moments logging the PETM interval in the Tibetan Himalaya.

Appendix A. Supplementary data

Supplementary data to this article can be found online at https://doi.org/10.1016/j.gloplacha.2023.104241.

References

Aubry, M.P., Ouda, K., Dupuis, C., William, A.B., Couvering, J.A.V., 2007. The Global Standard Stratotype-section and Point (GSSP) for the base of the Eocene Series in the Dababiya section (Egypt). Episodes 30 (4), 271–286.

Banner, J.L., Hanson, G.N., 1990. Calculation of simultaneous isotopic and trace element variations during water-rock interaction with applications to carbonate diagenesis. Geochim. Cosmochim. Acta 54, 3123–3137.

Bansal, U., Banerjee, S., Pande, K., Arora, A., Meena, S.S., 2017. The distinctive compositional evolution of glauconite in the cretaceous Ukra Hill Member (Kutch basin, India) and its implications. Mar. Pet. Geol. 82, 97–117.

Barnet, J.S., Littler, K., Westerhold, T., Kroon, D., Leng, M.J., Bailey, I., Zachos, J.C., 2019. A high-Fidelity benthic stable isotope record of late Cretaceous-early Eocene climate change and carbon-cycling. Paleoceanogr. Paleoclimatol. 34 (4), 672–691.

Bé, A.W., 1977. An ecological, zoogeographic and taxonomic review of recent planktonic foraminifera. In: Oceanic Micropaleontology. Academic Press, pp. 1–100.

Berndt, C., Planke, S., Alvarez Zarikian, C.A., Frieling, J., Jones, M.T., Millett, J.M., Yager, S.L., 2023. Shallow-water hydrothermal venting linked to the Palaeocene–Eocene Thermal Maximum. Nat. Geosci. 1-7.

Bosboom, R., Dupont-Nivet, G., Houben, A., Brinkhuis, H., Villa, G., Mandic, O., Stoica, M., Zachariasse, W., Guo, Z., Li, C., Krijgsman, W., 2011. Late Eocene Sea retreat from the Tarim Basin (West China) and concomitant Asian paleoenvironmental change. Palaeogeogr. Palaeoclimatol. Palaeoecol. 299 (3), 385–398.

Bosboom, R., Dupont-Nivet, G., Grothe, A., Brinkhuis, H., Villa, G., Mandic, O., Stoica, M., Kouwenhoven, T., Huang, W., Yang, W., Guo, Z., 2014. Timing, cause and

impact of the late Eocene stepwise sea retreat from the Tarim Basin (West China). Palaeogeogr. Palaeoclimatol. Palaeoecol. 403, 101–118.
Bowen, G.J., Zachos, J.C., 2010. Rapid carbon sequestration at the termination of the Palaeocene–Eocene Thermal Maximum. Nat. Geosci. 3 (12), 866–869.
Cao, W., Xi, D., Melinte-Dobrinescu, M.C., Jiang, T., Wise-Jr, S.W., Wan, X., 2018. Calcareous nannofossil changes linked to climate deterioration during the Paleocene-Eocene thermal maximum in Tarim Basin, NW China. Geosci. Front. 9 (5), 1465–1478.
Carmichael, M.J., Inglis, G.N., Badger, M.P., Naafs, B.D., Behrooz, L., Remmelzwaal, S., Monteiro, F.M., Rohrssen, M., Farnsworth, A., Buss, H.L., 2017. Hydrological and associated biogeochemical consequences of rapid global warming during the Paleocene-Eocene thermal Maximum. Glob. Planet. Chang. 157, 114–138.
Carmichael, M.J., Pancost, R.D., Lunt, D.J., 2018. Changes in the occurrence of extreme precipitation events at the Paleocene Eocene thermal maximum. Earth Planet. Sci. Lett. 501, 24–36.
Chen, Z., Wang, X., Hu, J., Yang, S., Zhu, M., Dong, X., Tang, Z., Peng, P., Ding, Z., 2014. Structure of the carbon isotope excursion in a high-resolution lacustrine Paleocene–Eocene Thermal Maximum record from central China. Earth Planet. Sci. Lett. 408, 331–340.
Chen, Z., Ding, Z., Yang, S., Zhang, C., Wang, X., 2016. Increased precipitation and weathering across the Paleocene-Eocene thermal Maximum in Central China. Geochem. Geophys. Geosyst. 17 (6), 2286–2297.
Chen, C., Guerit, L., Foreman, B.Z., Hassenruck-Gudipati, H.J., Adatte, T., Honegger, L., Perret, M., Sluijs, A., Castelltort, S., 2018. Estimating regional flood discharge during Palaeocene-Eocene global warming. Sci. Rep. 8, 1–8.
Church, J.A., Roemmich, D., Domingues, C.M., Willis, J.K., White, N.J., Gilson, J.E., Stammer, D., Köhl, A., Chambers, D.P., Landerer, F.W., Marotzke, J., Gregory, J.M., Suzuki, T., Cazenave, A., Le Traon, P.Y., 2010. Ocean temperature and salinity contributions to global and regional sea-level change. In: Church, J.A., Woodworth, P.L., Aarup, T., Wilson, W.S. (Eds.), Understanding Sea-Level Rise and Variability, 1st ed. Wiley-Blackwell, Chichester, pp. 143–176.
Conrad, C.P., 2013. The solid Earth's influence on sea-level. Geol. Soc. Am. Bull. 125 (7–8), 1027–1052.
Cui, Y., Kump, L.R., Ridgwell, A.J., Charles, A.J., Junium, C.K., Diefendorf, A.F., Freeman, K.H., Urban, N.M., Harding, I.C., 2011. Slow release of fossil carbon during the Palaeocene-Eocene thermal Maximum. Nat. Geosci. 4 (7), 481–485.
Davies, A., Gréselle, B., Hunter, S.J., Baines, G., Robson, C., Haywood, A.M., van Buchem, F.S., 2020. Assessing the impact of aquifer-eustasy on short-term cretaceous sea-level. Cretac. Res. 112, 104445.
DeConto, R., Pollard, D., 2003. A coupled climate-ice sheet modeling approach to the early Cenozoic history of the Antarctic ice sheet. Palaeogeogr. Palaeoclimatol. Palaeoecol. 198, 39–52.
Deconto, R., Pollard, D., 2016. Contribution of Antarctica to past and future sea-level rise. Nature 531, 591–597.
Dickens, G.R., Castillo, M.M., Walker, J.C., 1997. A blast of gas in the latest Paleocene: Simulating first-order effects of massive dissociation of oceanic methane hydrate. Geology 25, 259–262.
D'Onofrio, R., Luciani, V., Dickens, G.R., Wade, B.S., Kirtland Turner, S., 2020. Demise of the planktic foraminifer genus Morozovella during the early Eocene climatic optimum: new records from ODP Site 1258 (Demerara rise, Western Equatorial Atlantic) and site 1263 (Walvis Ridge, South Atlantic). Geosciences 10 (88), 1–22.
Dunham, R.J., 1962. Classification of carbonate rocks according to deposition texture. In: Ham, W.E. (Ed.), Classification of Carbonate Rocks, vol. 1. American Association of Petroleum Geologists, pp. 108–121.
Dupuis, C., Aubry, M.P., Steurbaut, E., Berggren, W.A., Ouda, K., Magioncalda, R., Cramer, B.S., Kent, D.V., Speijer, R.P., Heilmann-Clausen, C., 2003. The Dababiya Quarry Section: Lithostratigraphy, clay mineralogy, geochemistry and paleontology. Micropaleontology 49, 41–59.
Embry, A.F., Klovan, J.E., 1971. A late Devonian reef tract on northeastern Banks Island, NWT. Bull. Can. Petrol. Geol. 19, 730–781.
Flügel, E., 2010. Microfacies of Carbonate Rocks: Analysis, Interpretation and Application. Springer Science, Business Media, New York, pp. 1–976.
Fornos, J.J., Forteza, V., Martinez-Taberner, A., 1997. Modern polychaete reefs in western Mediterranean lagoons: Ficopomatus enigmaticus (Fauvel) in the Albufera of Menorca, Balearic Islands. Palaeogeogr. Palaeoclimatol. Palaeoecol. 128, 175–186.
Garzanti, E., 1991. Non-carbonate intrabasinal grains in arenites; their recognition, significance, and relationship to eustatic cycles and tectonic setting. J. Sediment. Res. 61 (6), 959–975.
Gavrilov, Y.O., Shcherbinina, E.A., Oberhänsli, H., 2003. Paleocene-Eocene boundary events in the northeastern Peri-Tethys. Geol. Soc. Am. 369, 147–168.
Gold, D.P., 2021. Sea-Level Change in Geological Time. In: Alderton, D., Elias, S.A. (Eds.), Encyclopedia of Geology, Second edition. Academic Press Publ, pp. 412–434.
Gutjahr, M., Ridgwell, A., Sexton, P.F., Anagnostou, E., Pearson, P.N., Palike, H., Norris, R.D., Thomas, E., Foster, G.L., 2017. Very large release of mostly volcanic carbon during the Palaeocene-Eocene Thermal Maximum. Nature 548 (7669), 573–577.
Hao, Y.C., Zeng, X.L., 1984. On the evolution of the West Tarim Gulf from Mesozoic to Cenozoic in terms of characteristics of foraminiferal fauna. Acta Micropalaeontogica Sin. 1 (1), 1–16 (in Chinese with English abstract).
Harding, I.C., Charles, A.J., Marshall, J.E.A., et al., 2011. Sea-level and salinity fluctuations during the Paleocene-Eocene thermal maximum in Arctic Spitsbergen. Earth Planet. Sci. 303 (1–2), 97–107.
Harris, A.D., Miller, K.G., Browning, J.V., et al., 2010. Integrated stratigraphic studies of Paleocene-lowermost Eocene sequences, New Jersey Coastal Plain: evidence for glacioeustatic control. Paleoceanography 25 (3), PA3211.
Hay, W.W., Leslie, M.A., 1990. Could possible changes in global groundwater reservoir cause eustatic sea-level fluctuations. In: Change, Sea-level (Ed.), National Research Council. National Academy Press, Washington DC, pp. 161–170.
Hu, X., Li, J., Han, Z., Li, Y., 2020. Two types of hyperthermal events in the Mesozoic-Cenozoic: Environmental impacts, biotic effects, and driving mechanisms. Sci. China Earth Sci. 63, 1041–1058.
Jackson, R., Carpenter, S., Dahm, C., McKnight, D., Naiman, R., Postel, S.L., Running, S., 2001. Water in a changing world. Ecol. Appl. 11 (4), 1027–1045.
Jiang, T., Wan, X., Aitchison, J.C., Xi, D., Cao, W., 2018. Foraminiferal response to the PETM recorded in the SW Tarim Basin, Central Asia. Palaeogeogr. Palaeoclimatol. Palaeoecol. 506, 217–225.
Jiang, J., Hu, X., Li, J., BouDagher-Fadel, M., Garzanti, E., 2021. Discovery of the Paleocene-Eocene thermal Maximum in shallow-marine sediments of the Xigaze forearc basin, Tibet: a record of enhanced extreme precipitation and siliciclastic sediment flux. Palaeogeogr. Palaeoclimatol. Palaeoecol. 562, 110095.
Jiang, J., Hu, X., Garzanti, E., Li, J., BouDagher-Fadel, M.K., Sun, G., Xu, Y., 2022. Enhanced storm-induced turbiditic events during early Paleogene hyperthermals (Arabian continental margin, SW Iran). Glob. Planet. Chang. 214, 103832.
John, C.M., Bohaty, S.M., Zachos, J.C., Zachos, J.C., Sluijs, A., Gibbs, S., Brinkhuis, H., Brolower, T.J., 2008. North American continental margin records of the Paleocene-Eocene thermal maximum: Implications for global carbon and hydrological cycling. Paleoceanography 23 (2), PA2217.
Jones, S.M., Hoggett, M., Greene, S.E., Jones, T.D., 2019. Large Igneous Province thermogenic greenhouse gas flux could have initiated Paleocene-Eocene thermal Maximum climate change. Nat. Commun. 10, 1–16.
Kaya, M.Y., Dupont-Nivet, G., Proust, J.N., Roperch, P., Bougeois, L., Meijer, N., Frieling, J., Fioroni, C., Altmer, S., Vardar, E., Barbolini, N., Stoica, M., Aminov, J., Mamtimin, M., Guo, Z.J., 2019. Paleogene evolution and demise of the proto-Paratethys Sea in Central Asia (Tarim and Tajik basins): Role of intensified tectonic activity at ca. 41 Ma. Basin Res. 34, 461–486.
Kaya, M.Y., Dupont-Nivet, G., Frieling, J., et al., 2022. The Eurasian epicontinental sea was an important carbon sink during the Palaeocene-Eocene thermal maximum. Commun. Earth Environ. 3 (1), 124.
Kelly, D.C., Nielsen, T.M., McCarren, H.K., Zachos, J.C., Röhl, U., 2010. Spatiotemporal patterns of carbonate sedimentation in the South Atlantic: Implications for carbon cycling during the Paleocene–Eocene thermal maximum. Palaeogeogr. Palaeoclimatol. Palaeoecol. 293 (1–2), 30–40.
Kennett, J.P., Stott, L.D., 1991. Abrupt deep-sea warming, palaeoceanographic changes and benthic extinctions at the end of the Palaeocene. Nature 353 (6341), 225–229.
Knauth, L.P., Kennedy, M.J., 2009. The late Precambrian greening of the Earth. Nature 460, 728–732.
Lan, X., Wei, J., 1995. Late Cretaceous–Early Tertiary Marine Bivalve Fauna from the Western Tarim Basin. Chinese Science Publishing House, Beijing.
Leckie, R.M., Olson, H.C., 2003. Foraminifera as proxies for sea-level change on siliciclastic margins. In: Olson, H.C., Leckie, R.M. (Eds.), Micropaleontologic Proxies for Sea-Level Change and Stratigraphic Discontinuities. SEPM Spec. Publ, Tulsa, Oklahoma, pp. 5–19 (no. 75).
Li, J., Hu, X., Garzanti, E., BouDagher-Fadel, M., 2017. Shallow-water carbonate responses to the Paleocene Eocene thermal maximum in the Tethyan Himalaya (southern Tibet): Tectonic and climatic implications. Palaeogeogr. Palaeoclimatol. Palaeoecol. 466, 153–165.
Li, M., Hinnov, L.A., Huang, C., Ogg, J.G., 2018. Sedimentary noise and sea levels linked to land–ocean water exchange and obliquity forcing. Nat. Commun. 9 (1), 1004.
Li, J., Hu, X., Zachos, J.C., Garzanti, E., BouDagher-Fadel, M., 2020. Sea level, biotic and carbon-isotope response to the Paleocene Eocene thermal maximum in Tibetan Himalayan platform carbonates. Glob. Planet. Chang. 194, 103316.
Li, J., Hu, X., Garzanti, E., BouDagher-Fadel, M., 2021a. Climate-driven hydrological change and carbonate platform demise induced by the Paleocene Eocene thermal Maximum (southern Pyrenees). Palaeogeogr. Palaeoclimatol. Palaeoecol. 567, 110250.
Li, W., Hu, X.M., Melinte-Dobrinescu, M.C., BouDagher-Fadel, M.K., Li, J., Zhang, S., Xu, Y., 2021b. Early Paleogene hyperthermal events and their environmental impacts in the Qimugen section, Tarim Sea. Chin. Sci. Bull. 66 (9), 1067–1082 (in Chinese with English abstract).
Li, M., Bralower, T.J., Kump, L.R., Self-Trail, J.M., Zachos, J.C., Rush, W.D., Robinson, M. M., 2022a. Astrochronology of the Paleocene-Eocene thermal Maximum on the Atlantic Coastal Plain. Nat. Commun. 13 (1), 5618.
Li, X., Hu, Y., Guo, J., Lan, J., Lin, Q., Bao, X., Yuan, S., Wei, M., Li, Z., Man, K., Yin, Z., Han, J., Zhang, J., Zhu, C., Zhao, Z., Liu, Y., Yang, J., Nie, J., 2022b. A high-resolution climate simulation dataset for the past 540 million years. Sci. Data 9 (1), 371.
Li, M., Zhang, H., Wang, M., Jin, Z., 2023. Astronomically forced changes in groundwater reservoirs and sea level during the greenhouse world. Chin. Sci. Bull. 68, 1517–1527 (in Chinese with English abstract).
Lovelock, J.E., 1979. Gaia, a New Look at Life on Earth. Oxford University Press, London.
McInerney, F.A., Wing, S.L., 2011. The Paleocene-Eocene thermal Maximum: a perturbation of carbon cycle, climate, and biosphere with implications for the future. Annu. Rev. Earth Planet. Sci. 39, 489–516.
Miller, K.G., Kominz, M.A., Browning, J.V., et al., 2005a. The Phanerozoic record of global sea-level change. Science 310 (5752), 1293–1298.
Miller, K.G., Wright, J.D., Browning, J.V., 2005b. Visions of ice sheets in a greenhouse world. Mar. Geol. 217 (3–4), 215–231.
Minshull, T.A., Marín-Moreno, H., Armstrong McKay, D.I., Wilson, P.A., 2016. Mechanistic insights into a hydrate contribution to the Paleocene-Eocene carbon cycle perturbation from coupled thermohydraulic simulations. Geophys. Res. Lett. 43 (16), 8637–8644.

Mount, J., 1985. Mixed siliciclastic and carbonate sediments: a proposed first-order textural and compositional classification. Sedimentology 32, 435–442.
Müller, R., Seton, M., Zahirovic, S., Williams, S., Matthews, K., Wright, N., Shephard, G., Maloney, K., Barnett-Moore, N., Hosseinpour, M., Bower, D., Cannon, J., 2016. Ocean basin evolution and global-scale plate reorganization events since Pangea breakup. Annu. Rev. Earth Planet. Sci. 44, 107–138.
National Oceanic and Atmospheric Administration (NOAA), 2023. Sea Levels Change Online. at. https://sealevel.nasa.gov/.
Panchuk, K., Ridgwell, A., Kump, L.R., 2008. Sedimentary response to Paleocene-Eocene thermal Maximum carbon release: a model-data comparison. Geology 36 (4), 315–318.
Peters, S.E., Loss, D.P., 2012. Storm and fair-weather wave base: A relevant distinction? Geology 40 (6), 511–514.
Pujalte, V., Robador, A., Payros, A., Sams o, J.M., 2016. A siliciclastic braid delta within a lower Paleogene carbonate platform (Ordesa-Monte Perdido National Park, southern Pyrenees, Spain): record of the Paleocene Eocene thermal maximum perturbation. Palaeogeogr. Palaeoclimatol. Palaeoecol. 459 (453), 470.
Pujalte, V., Schmitz, B., Payros, A., 2022. A rapid sedimentary response to the Paleocene-Eocene thermal Maximum hydrological change: New data from alluvial units of the Tremp-Graus Basin (Spanish Pyrenees). Palaeogeogr. Palaeoclimatol. Palaeoecol. 589, 110818.
Rovere, A., Stocchi, P., Vacchi, M., 2016. Eustatic and relative sea level changes. Curr. Clim. Change Rep. 2 (4), 221–231.
Sames, B., Wagreich, M., Wendler, J.E., Haq, B.U., Conrad, C.P., Melinte-Dobrinescu, M. C., Hu, X., Wendler, I., Wolfgring, E., Yilmaz, I.Ö., Zorina, S.O., 2016. Review: short-term sea-level changes in a greenhouse world — A view from the cretaceous. Palaeogeogr. Palaeoclimatol. Palaeoecol. 441, 393–411.
Sames, B., Wagreich, M., Conrad, C.P., Iqbal, S., 2020. Aquifer-eustasy as the main driver of short-term sea-level fluctuations during cretaceous hothouse climate phases. Geol. Soc. Lond. Spec. Publ. 498 (1), 9–38.
Saunders, A.D., Fitton, J.G., Kerr, A.C., Norry, M.J., Kent, R.W., 1997. The North Atlantic igneous province. Geophys. Monogr. Am. Geophys. Union 100, 45–94.
Schmitz, B., Pujalte, V., 2003. Sea-level, humidity, and land-erosion records across the initial Eocene thermal maximum from a continental-marine transect in northern Spain. Geology 31 (8), 689–692.
Scholle, P.A., Ulmer-Scholle, D.S., 2003. A Color Guide to the Petrography of Carbonate Rocks: Grains, Textures, Porosity, Diagenesis. AAPG Memoir 77, Tulsa, Oklahoma, USA, pp. 1–459.
Scholle, P., Bebout, D., Moore, C., 1983. Carbonate Depositional Environments. AAPG Memoir 77, Tulsa, Oklahoma, USA, pp. 1–691.
Schulte, P., Scheibner, C., Speijer, R.P., 2011. Fluvial discharge and sea-level changes controlling black shale deposition during the Paleocene–Eocene Thermal Maximum in the Dababiya Quarry section, Egypt. Chem. Geol. 285 (1–4), 167–183.
Scotese, C.R., 2021. An atlas of Phanerozoic paleogeographic maps: the seas come in and the seas go out. Annu. Rev. Earth Planet. Sci. 49, 679–728.
Self-Trail, J.M., Powars, D.S., Watkins, D.K., Wandless, G.A., 2012. Calcareous nannofossil assemblage changes across the Paleocene–Eocene Thermal Maximum: Evidence from a shelf setting. Mar. Micropaleontol. 92, 61–80.
Sluijs, A., Schouten, S., Pagani, M., et al., 2006. Subtropical Arctic Ocean temperatures during the Palaeocene/Eocene thermal maximum. Nature 441 (7093), 610–613.
Sluijs, A., Brinkhuis, H., Crouch, E.M., et al., 2008. Eustatic variations during the Paleocene-Eocene greenhouse world. Paleoceanography 23 (4), PA4216.
Sluijs, A., Van Roij, L., Harrington, G.J., et al., 2014. Warming, euxinia and sea level rise during the Paleocene–Eocene Thermal Maximum on the Gulf Coastal Plain: implications for ocean oxygenation and nutrient cycling. Clim. Past 10 (4), 1421–1439.
Smith, J., Hasiotis, S., Kraus, M., Woody, D., 2009. Transient dwarfism of soil fauna during the Paleocene–Eocene Thermal Maximum. Proc. Natl. Acad. Sci. 106 (42), 17655–17660.
Smith, T., Dupuis, C., Folie, A., Quesnel, F., Storme, J.Y., Iacumin, P., Riveline, J., Missiaen, P., Ladevèze, S., Yans, J., 2011. A new terrestrial vertebrate site just after the Paleocene–Eocene boundary in the Mortemer Formation of Upper Normandy, France. Compt. Rend. Palevol. 10 (1), 11–20.
Speijer, R.P., Morsi, A.M.M., 2002. Ostracode turnover and sea-level changes associated with the Paleocene-Eocene thermal maximum. Geology 30 (1), 23–26.
Speijer, R., Wagner, T., 2002. Sea-level changes and black shales associated with the late Paleocene thermal maximum: Organic-geochemical and micropaleontologic evidence from the southern Tethyan margin (Egypt-Israel). Geol. Soc. Am. 356, 533–549.
Speijer, R., Scheibner, C., Stassen, P., Morsi, A., 2012. Response of marine ecosystems to deep-time global warming: A synthesis of biotic patterns across the Paleocene-Eocene thermal maximum (PETM). Aust. J. Earth Sci. 105 (1), 6–16.
Sreenivasan, S.P., Samanta, A., BouDagher-Fadel, M., Mukherjee, S., Vadlamani, R., Bera, M.K., 2022. Increasing primary productivity in the oligotrophic Tethyan coastal ocean during the Paleocene-Eocene warming episode. Glob. Planet. Chang. 216, 103898.
Storey, M., Duncan, R.A., Tegner, C., 2007. Timing and duration of volcanism in the North Atlantic Igneous Province: Implications for geodynamics and links to the Iceland hotspot. Chem. Geol. 241 (3–4), 264–281.
Sun, J., Jiang, M., 2013. Eocene seawater retreat from the Southwest Tarim Basin and implications for early Cenozoic tectonic evolution in the Pamir Plateau. Tectonophysics 588, 27–38.
Sun, J., Windley, B.F., Zhang, Z., Fu, B., Li, S., 2016. Diachronous seawater retreat from the southwestern margin of the Tarim Basin in the late Eocene. J. Asian Earth Sci. 116, 222–231.
Svensen, H., Planke, S., Malthe-Sørenssen, A., Jamtveit, B., Myklebut, R., Eidem, T.R., Rey, S.S., 2004. Release of methane from a volcanic basin as a mechanism for initial Eocene global warming. Nature 429 (6991), 542–545.
Tang, T., Yang, H., Lan, X., Yu, C., Xue, Y., Zhang, Y., Hu, L., Zhong, S., Wei, J., 1989. Marine Late Cretaceous and Early Tertiary Stratigraphy and Petroleum Geology in Western Tarim Basin, China. Chinese Science Publishing House, Beijing (in Chinese with English abstract).
Tang, T., Xue, Y., Yu, C., 1992. Marine Sedimentary Characteristics and Sedimentary Environment of Upper Cretaceous to Lower Tertiary in the Western Tarim Basin, Xinjiang. Science Press, Beijing (in Chinese with English abstract).
Tapia, R., Le, S., Ho, S.L., et al., 2022. Planktic-benthic foraminifera ratio (%P) as a tool for the reconstruction of paleobathymetry and geohazard: A case study from Taiwan. Mar. Geol. 453, 106922.
Teng, X., Wang, C., Liu, C., Yan, K., Luo, Z., 2021. Paleocene-Eocene thermal Maximum lacustrine sediments in deep drill core SKD1 in the Jianghan Basin: A record of enhanced precipitation in Central China. Glob. Planet. Chang. 205, 103620.
Tierney, J., Zhu, J., Li, M., Ridgwell, A., Hakim, G., Poulsen, C., Whiteford, R., Rae, J., Kump, L., 2022. Spatial patterns of climate change across the Paleocene–Eocene Thermal Maximum. Proc. Natl. Acad. Sci. 119 (42), e2205326119.
Torfstein, A., Winckler, G., Tripati, A., 2010. Productivity feedback did not terminate the Paleocene-Eocene thermal Maximum (PETM). Clim. Past 6 (2), 265–272.
Tripati, A., Elderfield, H., 2005. Deep-sea temperature and circulation changes at the Paleocene-Eocene thermal Maximum. Science 308, 1894–1898.
Urey, H.C., 1947. The thermaldynamic properties of isotopic substances. J. Chem. Soc. 562–581.
Van der Zwaan, G., Jorissen, F., De Stigter, H., 1990. The depth dependency of planktonic/benthic foraminiferal ratios: constraints and applications. Mar. Geol. 95, 1–16.
Vitek, N.S., Morse, P.E., Boyer, D.M., Strait, S.G., Bloch, J.I., 2021. Evaluating the responses of three closely related small mammal lineages to climate change across the Paleocene–Eocene thermal maximum. Paleobiology 47 (3), 464–486.
Wang, M., Chen, H., Huang, C., Kemp, D., Xu, T., Zhang, H., Li, M., 2020. Astronomical forcing and sedimentary noise modeling of lake-level changes in the Paleogene Dongpu Depression of North China. Earth Planet. Sci. Lett. 535, 116116.
Wang, Y.S., Cui, Y., Su, H., Jiang, J.X., Wang, Y., Yang, Z.L., Hu, X.M., Jiang, S.J., 2022a. Response of calcareous nannoplankton to the Paleocene–Eocene Thermal Maximum in the Paratethys Seaway (Tarim Basin, West China). Glob. Planet. Chang. 217, 103918.
Wang, X., Xi, D., Watkins, D.K., Self-Trail, J.M., Tang, Z., Cao, W., Jiang, T., Kamran, M., Wan, X., 2022b. Regression of the Tethys Sea (Central Asia) during middle to late Eocene: evidence from calcareous nannofossils of western Tarim Basin, NW China. Mar. Micropaleontol. 171, 102085.
Wang, X., Xi, D., Mattioli, E., Wang, G., Wan, X., 2023. Middle Paleocene-early Eocene inter-regional correlations and palaeoclimatic changes in eastern Tethys Sea: Calcareous nannofossil evidence for Paleocene-Eocene Thermal Maximum (PETM) and sea-level change from the western Tarim Basin, NW China. Palaeogeogr. Palaeoclimatol. Palaeoecol. 626, 111672.
Westerhold, T., Marwan, N., Drury, A.J., Liebrand, D., Agnini, C., Anagnostou, E., Zachos, J.C., 2020. An astronomically dated record of Earth s climate and its predictability over the last 66 million years. Science 369 (6509), 1383–1387.
Widlansky, M.J., Long, X., Schloesser, F., 2020. Increase in sea level variability with ocean warming associated with the nonlinear thermal expansion of seawater. Commun. Earth Environ. 1 (1), 9, 1-12.
Wigley, T., Raper, S., 1987. Thermal expansion of sea water associated with global warming. Nature 330 (6144), 127–131.
Wing, S.L., Harrington, G.J., Smith, F.A., Bloch, J.I., Boyer, D.M., Freeman, K.H., 2005. Transient floral change and rapid global warming at the Paleocene-Eocene boundary. Science 310, 993–996.
Xi, D., Tang, Z., Wang, X., Qin, Z., Cao, W., Jiang, T., Wu, B., Su, Y., Zahang, Y., Muhammad, K., Fang, X., Wang, X., 2020. Cretaceous–Paleogene marine stratigraphy framework and its records of significant geologic events in the western Tarim Basin. Earth Sci. Front. 27 (6), 165–198 (in Chinese with English abstract).
Xie, Y., Wu, F., Fang, X., 2022. A transient south subtropical forest ecosystem in Central China driven by rapid global warming during the Paleocene-Eocene thermal Maximum. Gondwana Res. 101, 192–202.
Yang, H., Shen, Q., Ran, Y., Li, C., Liang, W., Yuan, S., Jin, C., 2018. Environmental magnetic records of PETM in the southwestern Sichuan Basin. Sci. Bull. 63 (9), 846–855.
Yao, W., Paytan, A., Wortmann, U.G., 2018. Large-scale Ocean deoxygenation during the Paleocene-Eocene thermal Maximum. Science 361 (6404), 804–806.
Zachos, J., Pagani, M., Sloan, L., Thomas, E., Billups, K., 2001. Trends, rhythms, and aberrations in global climate 65 Ma to present. Science 292, 686–693.
Zachos, J.C., Rohl, U., Schellenberg, S.A., Sluijs, A., Hodell, D.A., Kelly, D.C., Kroon, D., 2005. Rapid acidification of the ocean during the Paleocene-Eocene thermal maximum. Science 308 (5728), 1611–1615.
Zachos, J.C., Schouten, S., Bohaty, S., Quattlebaum, T., Sluijs, A., Brinkhuis, H., Gibbs, S. J., Bralower, T.J., 2006. Extreme warming of mid-latitude coastal ocean during the Paleocene-Eocene thermal Maximum: inferences from TEX86 and isotope data. Geology 34, 737–740.
Zeebe, R.E., Lourens, L.J., 2019. Solar System chaos and the Paleocene–Eocene boundary age constrained by geology and astronomy. Science 365, 926–929.
Zhang, S.J., Hu, X.M., Han, Z., Li, J., Garzanti, E., 2018. Climatic and tectonic controls on Cretaceous-Palaeogene Sea-level changes recorded in the Tarim epicontinental sea. Palaeogeogr. Palaeoclimatol. Palaeoecol. 501, 92–110.